Construction and Building Materials 525 (2026) 146359

Contents lists available at ScienceDirect

Construction and Building Materials

journal homepage: www.elsevier.com/locate/conbuildmat

Evaluation of methods for characterizing cement types in residual cementitious fines (RCF) from end-of-life concrete

A.T.M. Alberda van Ekenstein [a,b,*], H.M. Jonkers [a], M. Ottelé [a]

[a] Materials & Environment Section, Dpt 3MD, Faculty of Civil Engineering and Geosciences, Delft University of Technology, Delft 2628 CN, the Netherlands
[b] Urban Mine B.V, Zaandam 1505 HS, the Netherlands

ARTICLE INFO

Keywords:
Circular concrete
Residual cementitious fines
Concrete recycling
Cement identification
Handheld X-ray fluorescence
X-ray diffraction
Fourier transform infrared spectroscopy
Thermogravimetric analysis
Selective dissolution

ABSTRACT

Concrete production is a major contributor to global CO_2 emissions, responsible for approximately 80% of the emissions in the construction sector. This high emission level is primarily due to the use of clinker, an energy-intensive component of cement. Reducing the environmental impact of concrete therefore depends on producing and reusing high-quality residual cementitious fines (RCF) derived from End-of-Life (EoL) concrete. The process of obtaining high-quality RCF begins before concrete demolition, where identifying the cement type in existing concrete is crucial for high-value downstream processing. This study explores the suitability of currently available methods for identifying binder types in (destructively obtained) RCF and evaluates which of these methods could potentially be suitable for non-destructive identification of binder types in the original concrete. The methods investigated include handheld X-ray fluorescence (HXRF), X-ray diffraction (XRD), Fourier transform infrared spectroscopy (FTIR), thermogravimetric analysis (TGA), titration and selective dissolution. To assess their binder type identification potential, RCF powder samples obtained from concretes of known composition were analysed first. Results show that all five methods can distinguish and identify three binder types (Portland cement, blast furnace slag cement and fly ash cement) based on variations in the chemical and mineralogical properties of the RCFs derived from their respective concretes. HXRF currently shows the greatest potential for rapid, non-destructive, in-situ identification of binder types present in EoL concrete, while XRD and FTIR also show potential.

1. Introduction

The environmental impact of concrete lies primarily in the cement type used for its production and more specifically in its clinker content. At least 80% of the carbon dioxide (CO_2) emissions from the concrete production process is attributed to clinker [1,2]. As a result, binders low in clinker content are being increasingly used, such as blast furnace slag- and fly ash based binders. However, the availability of these materials is decreasing due to increased recycling of steel and closure of coal-fired electricity plants resulting in a decreased production of slag and fly ash, respectively [3]. The growing demand for low-carbon concrete coupled with declining SCM supplies will inevitably increase clinker demand. A possible technically viable strategy for enabling net reduction in primary clinker production while at the same time matching demands could lie in recovery and reuse of clinker and useful cementitious binders from End-of-Life (EoL) concrete [4]. However, recovery value depends on the cement type: clinker-rich cements like CEM I yield substantial amounts of clinker, whereas blended cements like CEM III/B contain considerably less. Therefore, concrete recycling should aim to recover a secondary binder that can replace primary cement, thereby reducing the consumption of virgin raw materials and at the same time the environmental footprint of concrete.

As the cement characteristics of residual cementitious fines (RCF) obtained from EoL concrete influences their potential for reuse, it is essential to already characterize this fraction before demolition in order to determine the best EoL concrete treatment strategies. The EN 197–1 identifies 27 products within the family of cementitious materials, which can be grouped into five main cement types: namely Portland cement (CEM I), Portland-composite cement (CEM II), blast furnace cement (CEM III), pozzolanic cement (CEM IV) and composite cement (CEM V) [5]. In the Netherlands, traditionally the most commonly used cement types are Portland cement (CEM I), Portland fly ash cement

* Corresponding author at: Materials & Environment Section, Dpt 3MD, Faculty of Civil Engineering and Geosciences, Delft University of Technology, Delft 2628 CN, the Netherlands
E-mail address: a.t.m.alberdavanekenstein@tudelft.nl (A.T.M. Alberda van Ekenstein).

https://doi.org/10.1016/j.conbuildmat.2026.146359
Received 18 November 2025; Received in revised form 13 March 2026; Accepted 13 April 2026
Available online 20 April 2026

(CEM II/B-V) and blast furnace cement (CEM III/B). With current scarcity of fly ash, Portland limestone cement (CEM II/A-LL) is gaining ground as well. All these cement types have their own specific properties and areas of application [6]. Currently, no distinction is made between cement types in EoL concrete prior to demolition. As a result, concrete waste is mixed regardless of its original cement composition, leading to a highly heterogeneous RCF fraction obtained after concrete crushing. This heterogeneity significantly reduces its reuse potential (Fig. 1). Moreover, mixing different concrete streams dilutes the clinker content in the recovered RCF. When clinker-rich streams (e.g. CEM I concrete) are combined with low-clinker streams (e.g. CEM III/B concrete), overall clinker concentration decreases. This is counterproductive, as clinker is the most valuable component in concrete. Selective demolition and separate processing by original cement type would therefore reduce heterogeneity while enabling recovery of clinker-enriched RCF streams with higher binding potential.

To obtain high-quality (more homogenous) residual cementitious fines and enhance its reuse potential, source separation strategies focused on discriminating the cement type and its quality present in EoL concrete are essential. A well established method for this is petrography, where EoL core samples are taken and prepared into thin sections for microscopic examination [7–9]. Even though this method accurately identifies cement types, it is destructive and time consuming [10,11], limiting its use for practical field application. As a result, there is growing interest in alternative approaches for on-site insight into the type and quality of binders present in EoL concrete. Rapid, non-destructive and portable identification techniques are particularly relevant for industrial application, as they could be integrated directly into demolition workflows without disrupting operations or requiring extensive sample preparation. During development of such methods, microscopic analysis can serve as verification when testing on unknown concrete samples. One promising method is the use of handheld X-ray fluorescence (HXRF), which is capable of identifying cement types and is already available in a portable format [12,13]. Its use in an industrial setting could enable demolition contractors and recyclers to rapidly screen concrete elements on-site, make informed real-time decisions on selective demolition, separate storage and directly assign concrete waste streams to the appropriate recycling or upcycling routes, transforming concrete recycling into a high value recovery process. Besides HXRF, other methods may also be of interest to gain further insight into the quality of the residual cementitious fines. Methods such as X-ray diffraction (XRD), Fourier transform infrared spectroscopy (FTIR), thermogravimetric analysis (TGA), titration, and selective dissolution may provide complementary information that can help to increase certainty of cement type identification and provide insight in other physical, chemical and mineralogical properties (i.e. contamination, non-hydrated particles, characteristics influencing upcycling approach) that can help to determine the most optimal EoL concrete recycling process [14–19]. However, most of these methods currently require laboratory conditions due to equipment size, sample preparation requirements or environmental constraints and are not yet available for application on-site in a practical setting. Understanding their potential for reliable cement type identification in laboratory settings is needed to evaluate which techniques warrant future development. Such evaluation is essential for prioritizing methods that can be translated into robust and scalable tools for routine industrial use. With continued technological advancements addressing the current limitations, these methods may become viable tools for binder identification prior to the demolition of End-of-Life concrete structure.

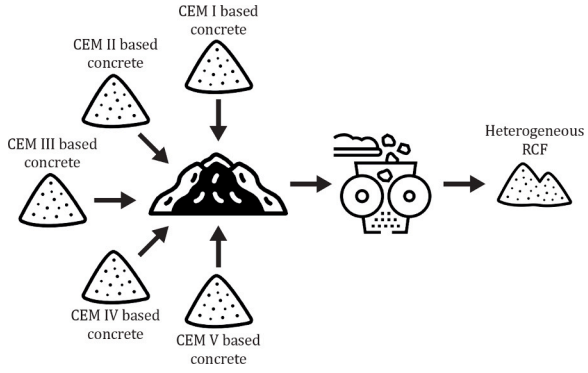

Fig. 1. Current EoL concrete crushing practice, where concrete waste streams with different cement types are mixed together resulting in heterogeneous residual cementitious fines.

The use of RCF as a cement replacement with or without prior treatment has been studied by multiple researchers [20–23]. In untreated and uncharacterized form, only relatively small replacement percentages of cement are possible while maintaining a strength comparable to that of the reference mixture, as RCF is typically regarded as an inert filler [22,24]. However, an activating effect of RCF has been observed when combined with blast furnace slag (BFS) [20,23], particularly RCF of high alkalinity (due to a large concentration of OH^- ions coming from calcium hydroxide) which can activate pozzolanic materials [25]. This underlines that specific RCF origin and composition are crucial for maximizing value in new concrete mixtures. CO_2 treatment methods are gaining attention for both their potential CO_2 storage in recycled concrete fractions and for their potential to produce reactive pozzolanic material. RCF originating from highly alkaline Portland cement (CEM I) are potentially effective for CO_2 capture due to elevated levels of residual alkalinity, while BFS-rich RCF appear to provide value as pozzolanic material as it demonstrates better carbonation performance than fly ash-rich RCF [3,26]. Thermal treatment is another promising upcycling method for RCF as it might restore initial binder potential, therefore being most valuable to potentially fully replace primary cement in concrete mixtures [21,27]. However, more research into RCF characterization is needed to optimize its value for replacing primary cement in concrete mixtures, either directly or after upcycling. A major obstacle is the heterogenous composition of RCF produced through traditional EoL concrete treatment methods as depicted in Fig. 1. Implementing source separation strategies could yield more homogeneous RCF from the EoL concrete crushing process, improving its value (highest application potential) either directly or indirectly after the most appropriate upcycling treatment. While previous RCF characterization studies have focused on gaining insight into the added value through treatment methods such as CO_2 curing or thermal activation [20,28], this research employs characterization primarily to identify the original cement type, enabling in-situ determination to facilitate targeted source separation.

With the introduction of EN 197–6 [29] in 2023, recycled concrete fines as a main component can partially replace 6–35% of clinker in new concrete mixtures, depending on the cement type and RCF properties. This percentage could increase when the binding capacity of the RCF is increased through proper selection and tailored upcycling methods, making EoL concrete source separation strategies with cement type identification an essential step in this process.

This study aims to assess the potential of various methods to rapidly identify the cement type present in EoL concrete before crushing. To evaluate which identifying methods show promise for this application, including those not currently available in portable form, the assessment was conducted on RCF powders obtained after crushing. RCF samples obtained from three different concrete blocks, differing only in cement type (Portland cement-, blast furnace slag cement- and fly ash (FA) cement based concrete), were analysed using a set of methods comprising: X-ray fluorescence, both stationary (XRF) and handheld (HXRF), X-ray diffraction (XRD), titration and selective dissolution, thermogravimetric analysis (TGA), differential scanning calorimetry (DSC), Fourier transform infrared spectroscopy (FTIR) and polarized and fluorescence microscopy. Further insight in the physical properties of RCF was obtained through measurement of the particle size

distribution and particle density. While several techniques included in this study are currently destructive and laboratory-based, they may provide the detailed information required for reliable binder identification that available non-destructive techniques cannot deliver. Furthermore, methods that are able to successfully identify binder types in powder samples could potentially be developed into portable, non-destructive alternatives for future in-situ application on concrete structures.

2. Materials and methods

2.1. Concrete blocks and production of residual cementitious fines

2.1.1. Concrete blocks

Concrete blocks were made to produce the RCF used in this study. The blocks were based on three different concrete mixtures (Table 1), which varied only in the cement type used. These cement types were selected based on the three most used cement types in the Netherlands: CEM I, CEM III/B and CEM II/B-V, which also represent some of the most dominant cement constituents (clinker, slag, fly ash) used across Europe [4]. The concrete blocks were produced by a commercial ready-mix concrete plant in Zaandam using their standard mix design practices. The cement types comply with EN 197–1 [5], which specifies approximately 70% GGBFS replacement in CEM III/B and 30% fly ash replacement in CEM II/B-V. From each mixture, five blocks measuring 160x80x80 cm were produced and placed in outdoor conditions. The blocks were subjected to outdoor weathering conditions for approximately 1.5 years to simulate realistic aging of concrete structures before demolition. Outdoor exposure can modify the concrete surface through processes such as erosion, moisture, efflorescence effect and surface contamination [30–32]. For the produced powder samples, these effects are expected to be limited, as the large volume of powder dilutes the impact on the overall chemical composition. After approximately 1.5 year the blocks were crushed to produce besides granulate also residual cementitious fines (RCF), i.e. the powder fractions further investigated in this study.

2.1.2. Crushing process

For crushing the concrete blocks, an innovative concrete crushing process (Fig. 2) was employed. While crushing processes have been demonstrated at laboratory scale in previous studies [33,34], this research employed the process at an industrial scale. In short, the blocks were crushed using a hydraulic excavator to produce a size of rubble suitable for further processing in the impact crusher. The impact crusher served as a pre-crusher, reducing the rubble to a maximum particle size of 55 mm. Since the concrete blocks used in this research were not exposed to other materials from a demolition site, the material was fed directly into an innovative crusher (the Smart Liberator) provided by Urban Mine B.V. This machine mechanically removed adhered cement paste from the aggregates by utilizing the difference in hardness between cement stone and aggregates, crushing only the cement while preserving the sand and gravel [35,36]. The process again resulted in two fractions: 0–4 mm and 4–22 mm. This specific 0–4 mm fraction contains the highest concentration of cementitious material. Therefore, this fraction was subsequently processed by an air separation technique (the Smart Refiner) provided by Urban Mine B.V., which further separated it into three fractions: a clean secondary sand fraction (0.25–4 mm) and two fine powder fractions (0–65 μm and 65–250 μm). In this study, the 0–65 μm fraction was selected for further analysis, as it is assumed to contain the majority of the original cementitious binder based on the applied production process. The analytical approach presented in this study is, however, considered applicable to other binder-enriched fractions obtained from different recycling processes. This fraction is hereafter referred to as the residual cementitious fine (RCF) fraction.

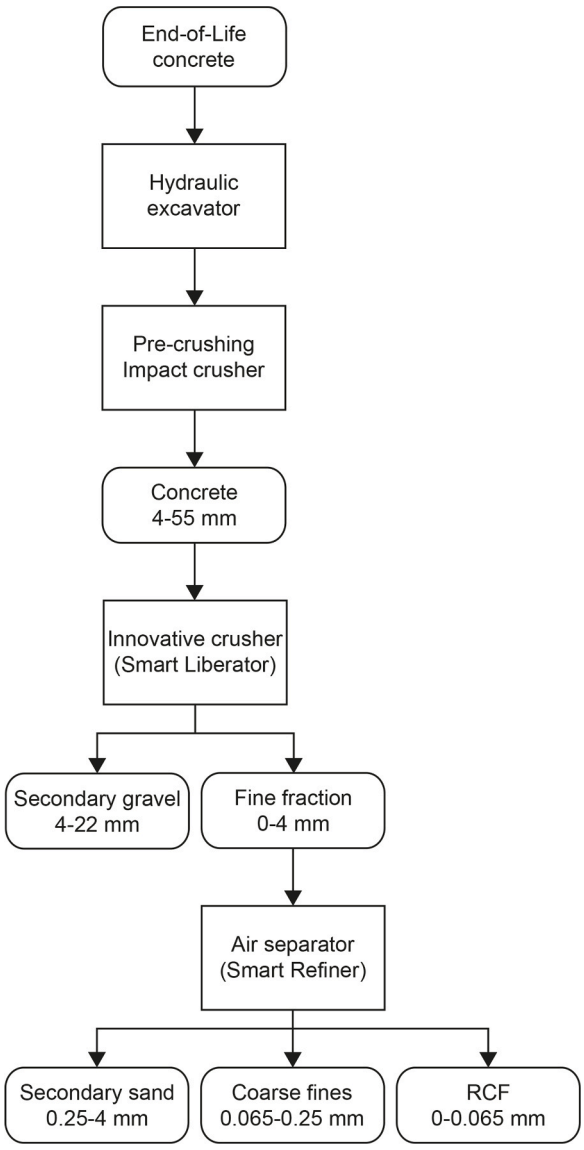

Fig. 2. Innovative concrete crushing an separation process for the production of secondary aggregates and RCF.

2.1.3. Materials

The RCF fractions obtained from the three types of concrete blocks are labeled as follows: Residual cementitious fines 1 (F1) from block 1,

Table 1
Mixture design of the concrete blocks with varying binder types.

	Concrete mix design [kg]							
	River gravel 4/32	River sand 0/4	CEM I 52.5 R	Ground granulated blast furnace slag	Fly ash	Masterglenium Sky 648	Water	Total
Block 1: CEM I	1010	860	330	0	0	2	162	2364
Block 2: CEM III/B	1010	860	100	230	0	2	162	2364
Block 3: CEM II/B-V	1010	830	230	0	100	2	162	2334

residual cementitious fines 2 (F2) from block 2 and residual cementitious fines 3 (F3) from block 3. As reference material three hydrated cement types were used, namely Portland cement hydrate (CEM I hydrate), blast furnace slag cement hydrate (CEM III/B hydrate), Portland – Fly ash cement hydrate (CEM II/B-V hydrate) and primary (non-hydrated) Portland cement were used. The hydrate reference specimens were made by mixing the cement types with water, using a water-binder ratio similar to what was applied for the concrete blocks (w/b = 0.49). These paste specimens isolate the characteristics of the studied cement types without the presence of aggregates, enabling clear identification of cement type-specific signatures in the analytical techniques used. The produced specimens were stored in closed trays for approximately 1.5 years, after which they were crushed to powders through milling and grinding using a Retsch mortar grinder RM200. Particles passing through a 63 μm sieve were collected and stored in sealed jars until further testing. An overview of the 7 powder fractions (RCF 1–3 plus 4 reference samples) prepared for further characterization are provided in Table 2.

2.2. Characterization and methods for identification

2.2.1. Particle size distribution

The particle size distribution of the samples was measured using an EyeTech Laser diffractometer. Powder samples were added to 500 ml ethanol until sufficient concentration was registered by the diffractometer. Ethanol was preferred over water, as the samples contained cementitious materials that would undergo hydration upon contact with water.

2.2.2. Density

Before determining the density, the powders were dried at 105 °C until constant mass was achieved. The moisture content was simultaneously determined following EN-1097–5 [37]. The density of the materials was determined with the Ultrapycnometer 5000. This is a pycnometer where helium gas is used to determine the volume of a sample. Average weight of the samples was 40 g.

2.2.3. X-ray fluorescence

The chemical composition of the samples was measured both by handheld- and desktop x-ray fluorescence (XRF). The handheld XRF (HXRF) used for these measurements was a X-MET8000 Expert GEO. It features a 25 mm^2 high resolution silicon-drift detector and a Rh target X-ray tube. The measurement spot size used was 10.7 × 9.4 mm. Measurement reliability and repeatability for this instrument can be found in [38].

For the desktop measurements, a Bruker S2 PUMA A35X1 ED-XRF system, containing a x-ray tube with an Ag anode and a Peltier cooled silicon drift detector, was used. Measurements were done on pressed pellets. These were made by mixing 4.00 g of the powder samples and 1.00 g Cereox from Fluxana as a binding agent. After mixing pressed pellets were prepared with a Vaneox pressing machine, using a load of 20 tons. The loss of ignition (LOI) was determined by igniting the samples in a BOF 1100 Carbolite Chamber Furnace at 950 °C for 1 h [39]. After ignition the samples were cooled in a desiccator until room temperature. Both the weight before (m1) and after ignition (m2) were recorded and used to determine the LOI by using the following formula:

$$LOI\,[\%] = \frac{m1 - m2}{m1} \times 100\% \quad (1)$$

2.2.4. X-ray diffraction

The crystalline phases in the samples was analysed using a Bruker D8 Advance Eco X-ray diffractometer with a LynxEye XE-T detector. The x-ray source used was a CU-tube with a Cu-Kα wavelength of 1.5418 Å. The voltage used was 40 kV and the x-ray beam current was set to 25 mA. The samples were scanned in the 2θ range, varying the angles between 5° and 75°.

2.2.5. Titration and selective dissolution

A titration and selective dissolution approach was developed to identify the binder type in the powder samples. For this purpose hydrochloric acid (HCl) was chosen as fly ash (Class F) does not dissolve in HCl, whereas Portland cement, blast furnace slag cement and their hydration products do [40]. For this analysis 20 g of each powder type was washed with a 4 M HCl solution (90 ml). After 30 min a black layer should be observed only for samples containing fly ash as all other cementitious materials dissolve. If no black layer is observed, a non-fly ash based binder type must have been present.

After determining whether any powder batches contained fly ash, a new set of samples from the non-fly ash batches was selected for further analysis using a titration setup based on the assumption that binders containing CEM I and CEM III/B require respectively high and low amounts of HCl to bring the pH of the alkaline material in suspension down to 7. A 2 M HCl titrant solution was used for the titration. An amount of 160 mg cementitious material was added to a 150 ml glass beaker together with 100 ml water. In order to compensate for contaminant sand (silicate) present in the RCF samples, the actual cementitious binder material fraction within the RCF sample was derived first from the HCL dissolution procedure applied in the previous fly ash determination test. The solid fraction of the RCF samples F1 and F2 (not containing fly ash) remaining after HCL dissolution was assumed to be the sand fraction as found in preliminary experiments. The weight of the RCF samples used for the HCL titration test was thus corrected for the present sand fraction in order to ensure that 160 mg of cementitious binder was present in these samples. During subsequent titration, 0.2 ml aliquots titrant was added until a pH of 7 was reached. The total volume of titrant added at this point was recorded.

2.2.6. Thermogravimetric analysis and differential scanning calorimetry

A Netzsch STA 449 F3 Jupiter was used to simultaneously perform thermogravimetric analysis (TGA) and differential scanning calorimetry (DSC). Samples were heated in an alumina crucible with cover under argon atmosphere. The temperature was increased from 40 to 1050 °C at a heating rate of 10 °C/min. These conditions as well as the same crucible with cover were used to determine a baseline, which was subtracted from the results. The amount of portlandite (CH; $Ca(OH)_2$) and calcite (CC^{-}; $CaCO_3$) were determined based on their decomposition reactions according to the following equations:

$$Ca(OH)_2 \rightarrow CaO + H_2O \quad (2)$$

$$CaCO_3 \rightarrow CaO + CO_2 \quad (3)$$

Table 2
Overview of the composition of the three RCF and four reference samples.

	Residual cementitious fines	Portland cement	Ground granulated blast furnace slag	Fly ash
Residual cementitious fines 1 (F1)	100%	-	-	-
Residual cementitious fines 2 (F2)	100%	-	-	-
Residual cementitious fines 3 (F3)	100%	-	-	-
CEM I	-	100%	-	-
CEM I hydrate	-	100%	-	-
CEM II/B-V hydrate	-	70%	-	30%
CEM III/B hydrate	-	30%	70%	-

$$m_{CH} = m_H \times \frac{74\frac{g}{mol}}{18\frac{g}{mol}} \quad (4)$$

$$m_{C\bar{C}} = m_{\bar{C}} \times \frac{100\frac{g}{mol}}{44\frac{g}{mol}} \quad (5)$$

Where m_{CH} is the content of CH, m_{CC^-} is the content of $C\bar{C}$ and m_H and m_{C^-} are the weight loss of water (H_2O) and carbon dioxide (CO_2) determined by TGA respectively.

2.2.7. Fourier transform infrared spectroscopy

Fourier transform infrared spectroscopy (FTIR) was used to gain insight into differences in the molecular structure between the various samples. FTIR spectra were measured with a Nicolet iS50 FT-IR in the range of 400–4000 cm^{-1}. A total of 24 scans were taken for every measurement at a resolution of 4 cm^{-1}. Powder samples were placed on the crystal at the top of machine and pressed down with the pressure anvil.

2.2.8. Polarized and fluorescence microscopy

Concrete cores with a diameter of 100 mm were taken from the concrete blocks and processed for the production of thin sections. In total three thin sections per block were produced. The thin sections were examined with an Axioscope 5 microscope in plane-polarized transmitted light.

3. Results

3.1. Physical properties

Visual observation of the powders showed differences in color between the three hydrated binder sample types. Fig. 3 shows that CEM I hydrate has the lightest color, whereas CEM II/B-V hydrate is the darkest. CEM III/B hydrate falls in between and has a more blueish tint. For the three RCF samples a comparable trend was observed. F1 (CEM I based) has the lightest color, followed by F2 (CEM III/B based) and F3 (CEM II/B-V based) is the darkest. Although the difference between F2 and F3 appeared less distinct.

The particle size distribution of the RCF- and the reference samples is shown in Fig. 4. The RCF samples showed a slightly increased coarser fraction compared to the hydrated reference cements. Additionally, unreacted CEM I showed the highest finest particle size fraction. Particle size parameters D(10), D(50) and D(90) can be found in Table 3, which confirm the observations from Fig. 4. Table 3 also shows the density of the powders. The density of the RCF samples was higher than that of the hydrated reference cements. F1 and F3 showed comparable densities, with the density of F1 being slightly higher. F2 showed the lowest density compared to the other residual cementitious fines. For the reference hydrates, CEM I hydrate also showed the highest density. CEM II/B-V hydrate and CEM III/B hydrate showed a lower but comparable density. Unreacted CEM I showed the highest density of all the materials. As the RCF samples can be composed of a combination of hydrated binder, non-hydrated binder and river sand, these are expected to show a higher variation in density in comparison to the reference specimens.

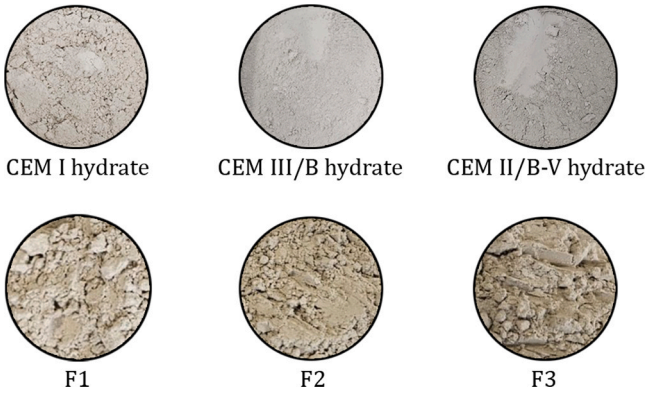

Fig. 3. Powder samples of the reference cements (top three) and the residual cementitious fines (bottom three). A difference in color can be observed.

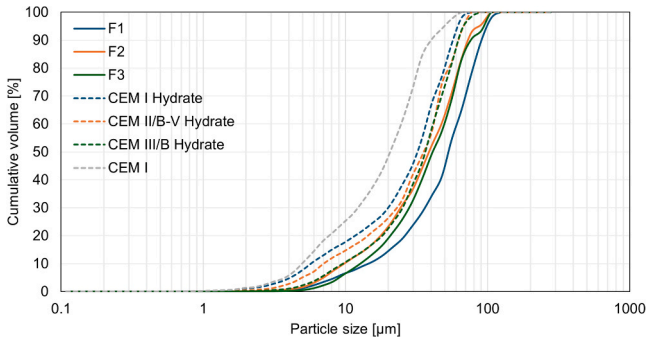

Fig. 4. Particle size distribution of residual cementitious fines F1, F2, F3 and the hydrated CEM I, CEM III/B, CEM II/B-V cements and non-hydrated CEM I cement.

3.2. Handheld and stationary X-ray fluorescence

Fig. 5 shows the chemical composition of the three RCF samples as measured by HXRF. A clear difference was observed between the three RCF types. F1 (CEM I based) showed an increase in CaO and a decrease in SiO_2 and Al_2O_3 compared to F2 (CEM III/B based) and F3 (CEM II/B-V based). Between F2 and F3, a lower CaO concentration and a higher SiO_2 concentration was observed for F2. Additionally, F2 showed the highest MgO concentration, whereas F3 showed the higher Fe_2O_3 concentration. These observations generally align with the deviations seen in the corresponding hydrated reference cement types (Fig. 6). However, the CEM III/B hydrate contained a higher amount of CaO and a lower amount of SiO_2 compared to the CEM II/B-V hydrate.

Based on the normalized average oxide concentrations (values normalized to 100%) of the RCF samples and the hydrated reference cement types, limits can be identified to distinguish between the cement types in the RCF samples. These limits are based on the oxides Fe_2O_3, Al_2O_3 and MgO. Concentrations of Fe_2O_3 larger than 3.4 correspond to the cement type CEM II/B-V, whereas MgO concentrations larger than 1.8 corresponds to CEM III/B. Al_2O_3 concentrations lower than 7.0 corresponds to CEM I.

Figs. 7 and 8 present normalized ratios between elements that can be used to identify the cement type within the RCF samples. A normalized value of Fe_2O_3/Al_2O_3 smaller than 40.00 is typical for cement type CEM III/B. After identifying CEM III/B, the other two cement types can be distinguished by using the ratio Fe_2O_3/CaO or Al_2O_3/CaO. When the normalized value of Fe_2O_3/CaO is smaller than 9.00 and that of Al_2O_3/CaO is smaller than 18.00, the cement type within the residual cementitious fines corresponds with CEM I.

Table 4 shows the normalized composition of the three RCF- and the four reference samples for both the HXRF and desktop XRF. Differences generally smaller than ±5.5% can be observed between the handheld and desktop XRF, which are therefore seen as comparable. Additionally, observed trends in the oxide composition are also similar (Appendix A).

3.3. X-ray diffraction

Observed differences in the mineralogical composition of the hydrated cement types CEM I, CEM III/B, CEM II/B-V and the unreacted

Table 3
Density, particle size parameters D(10), D(50) and D(90), moisture content and loss of ignition of the residual cementitious fines and the references cement samples.

Material	Density [g/cm^3]	D(10) [μm]	D(50) [μm]	D(90) [μm]	Standard deviation [μm]	Moisture content [%]	LOI including moisture content [%]
F1	2.332	13.42	48.67	84.78	25.72	11.2	21.0
F2	2.251	9.09	35.35	68.29	22.13	10.8	18.5
F3	2.329	11.70	37.82	70.79	22.83	14.2	23.5
CEM I hydrate	2.211	5.31	29.55	53.66	17.01	11.4	29.3
CEM II/B-V hydrate	2.186	6.52	32.61	57.84	17.86	13.7	28.8
CEM III/B hydrate	2.190	8.75	33.57	55.23	17.31	13.6	26.1
CEM I	3.067	4.57	19.12	36.68	12.78	-	2.7

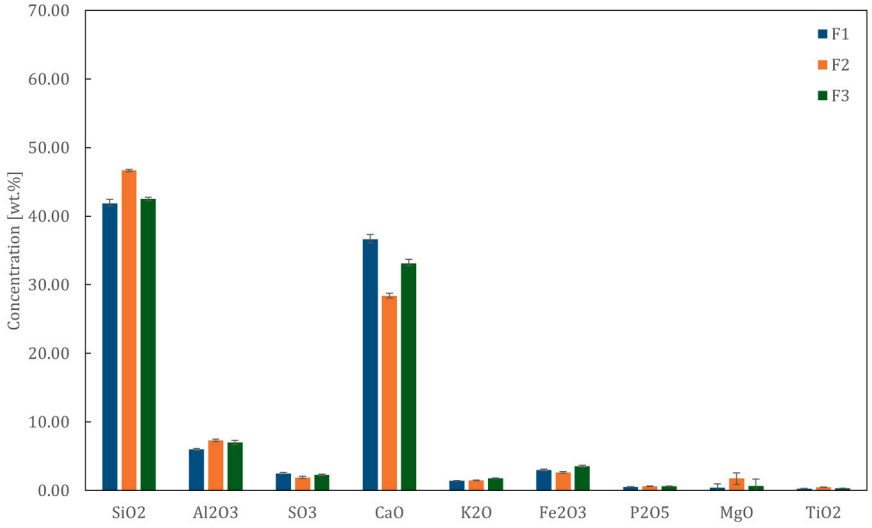

Fig. 5. Chemical composition measured by HXRF of the residual cementitious λ.

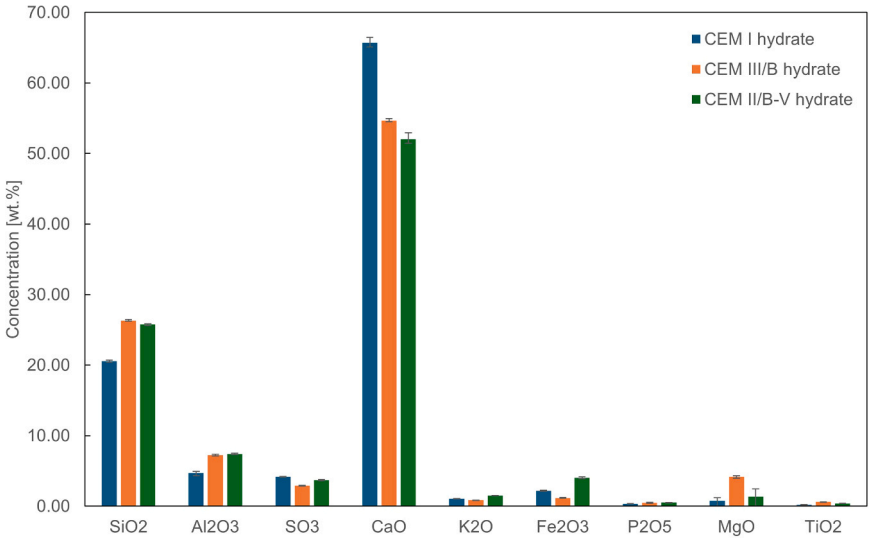

Fig. 6. Chemical composition measured by HXRF of the hydrated primary reference cement types CEM I, CEM III/B and CEM II/B-V.

CEM I as characterized by XRD are illustrated in Fig. 9. For the hydrates CEM I has the most distinct portlandite peaks, followed by CEM II/B-V and CEM III/B. Other differences that can be observed are the apparent presence of mullite and quartz in CEM II/B-V, hydrotalcite in both CEM III/B and CEM II/B-V and the more amorphous and less distinct peaks of CEM III/B. Unreacted CEM I contains the four major phases alite (C3S), belite (C2S), aluminate phase (C3A) and ferrite phase (C4AF), but a small number of peaks also show the presence of anhydrite and calcite.

In the diffraction patterns of the RCF samples (Fig. 10) quartz peaks are visible, which indicate the presence of sand. In the case of F3 (CEM II/B-V based), the quartz can be a combination of fine sand particles and quartz from the fly ash. Except for the presence of quartz comparable trends that were observed in the reference cements, can also be seen in the corresponding RCF samples. F1 (CEM I based) has the most distinct portlandite peaks, small mullite peaks are present in F3 and hydrotalcite is observed for both F2 (CEM III/B based) and F3. Similar crystalline phases such as quartz, calcite and portlandite have also been reported in XRD analyses of recycled aggregate concrete and modified cement systems in previous studies [41,42]. However, the present results further

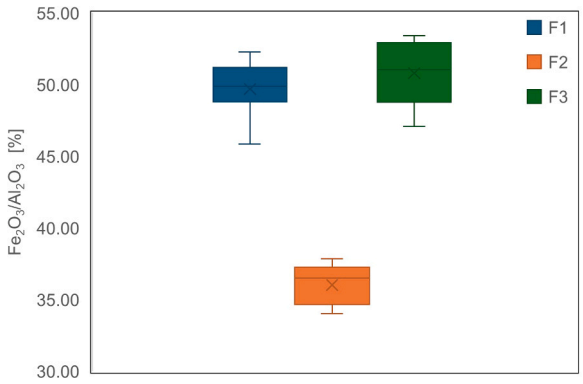

Fig. 7. Normalized oxide ratio Fe_2O_3/Al_2O_3 to identify the presence of CEM III/B as the cement type in the residual cementitious fines.

highlight differences in phase assemblage related to the specific binder compositions used in this study.

3.4. Titration and selective dissolution

The three RCF samples were washed with HCl to determine the presence of fly ash (Class F) and to estimate the amount of sand present. Fig. 11 shows the occurrence of a black layer for RCF sample F3 (CEM II/B-V based). Upon exposure to a magnet, this black layer is attracted to the magnet, demonstrating magnetic properties (Fig. 12). For both RCF F1 (CEM I based) and RCF F2 (CEM III/B based) no black layer was observed and the remaining material was weighed to estimate the sand content within these samples. The sand content was then used to calculate the amount of material required for the titration experiments. Table 5 shows these results.

After identifying the sample containing fly ash, the other two samples were further analysed through HCl titration. Initial measurements revealed that CEM I hydrate required 1.5 ml (±0.1 ml) of 2 M HCl to maintain a pH below 7, while CEM III/B hydrate required only 1.0 ml (±0.2 ml). This difference in HCl consumption indicates that acid titration can differentiate between these two cement types. Fig. 13 shows the change in pH over a certain time period during addition of HCl to the solution containing RCF until the pH stabilized below 7. The figures show that RCF sample F1 (CEM I based) required more (5 times 0.2 ml aliquots) HCl to keep the pH below 7 for more than one hour compared to F2, for which 4 times 0.2 ml aliquots were sufficient. In addition, the pH increased faster after HCl aliquot additions in the RCF sample F1 solution. Indicating that the alkaline buffering capacity was higher than that of RCF sample F2 (see also Table 6).

3.5. Thermogravimetric analysis and differential scanning calorimetry

Figs. 14 and 15 show the TGA and DTG curves of the reference cement- and the RCF samples. In both figures the curves show an abrupt weight loss at three temperature ranges. Between 40 and 250 °C the first large weight loss is the result of the evaporation of free water and the dehydration of hydration products such as ettringite, monosulfate and calcium silicate hydrate (C-S-H) [43,44]. The second abrupt weight loss occurs between 400 and 550 °C as a result of the decomposition of portlandite ($Ca(OH)_2$; CH) [43,45]. The final transition due to the decomposition of calcite ($CaCO_3$) takes place in the range 700–900 °C [43]. Between 250 and 400 °C and 550–700 °C a gradual weight loss is observed as the C-S-H, calcium aluminate hydrates and other minor hydrates continue to dehydrate [46,47].

Differences can be observed between the primary hydrated reference cements in Fig. 14, especially for the abrupt weight loss related to CH and calcite. The largest weight loss between 400 and 550 °C is observed

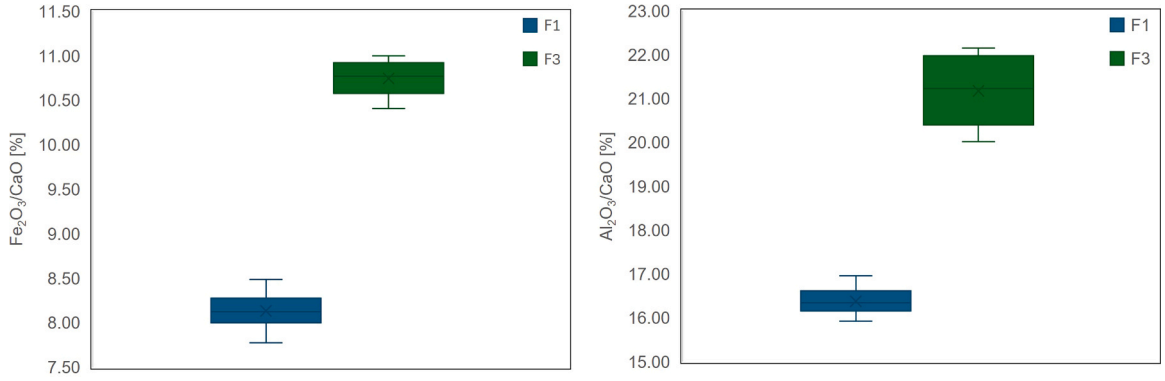

Fig. 8. Normalized oxide ratio Fe_2O_3/CaO and Al_2O_3/CaO to distinguish the presence of CEM I or CEM II/B-V as a cement type in the residual cementitious fines.

Table 4
Normalized oxide content of residual cementitious fines F1, F2 and F3 and primary cement types.

	F1		F2		F3		CEM I hydrate		CEM II/B-V hydrate		CEM III/B hydrate		CEM I unreacted	
	HXRF	XRF	HXRF	XRF	HXRF	XRF	HXRF	XRF	HXRF	XRF	HXRF	XRF	HXRF	XRF
SiO2	44.97	48.17	50.87	54.10	46.01	51.26	20.51	18.58	26.46	27.47	26.54	28.04	21.61	17.04
Al2O3	6.44	7.04	7.99	8.86	7.59	8.50	4.69	5.17	7.59	9.47	7.32	9.05	5.12	4.91
SO3	2.68	2.46	2.04	2.00	2.48	2.32	4.15	4.05	3.80	3.59	2.94	2.95	6.49	5.03
CaO	39.35	35.51	30.93	26.90	35.84	30.60	65.53	66.86	53.46	51.41	55.20	51.53	62.09	67.59
K2O	1.52	1.15	1.59	1.12	1.90	1.41	1.07	0.95	1.55	1.35	0.86	0.72	1.19	0.96
Fe2O3	3.20	3.32	2.88	2.81	3.85	3.69	2.18	2.50	4.12	4.46	1.19	1.10	1.90	2.52
P2O5	0.56	n.d.	0.65	n.d.	0.65	n.d.	0.32	n.d.	0.53	n.d.	0.46	n.d.	0.22	n.d.
MgO	0.43	1.65	1.96	3.32	0.72	1.51	0.79	1.16	1.39	1.29	4.22	5.46	0.66	1.16
TiO2	0.30	0.41	0.52	0.61	0.37	0.46	0.20	0.28	0.41	0.53	0.61	0.73	0.21	0.29
Cl	0.24	0.06	0.28	0.04	0.29	0.04	0.14	0.10	0.23	0.07	0.20	0.04	0.10	0.11
MnO	0.12	0.10	0.16	0.15	0.12	0.09	0.11	0.11	0.12	0.10	0.23	0.23	0.10	0.11
SrO	0.18	0.13	0.12	0.09	0.20	0.13	0.30	0.24	0.34	0.25	0.22	0.15	0.31	0.27

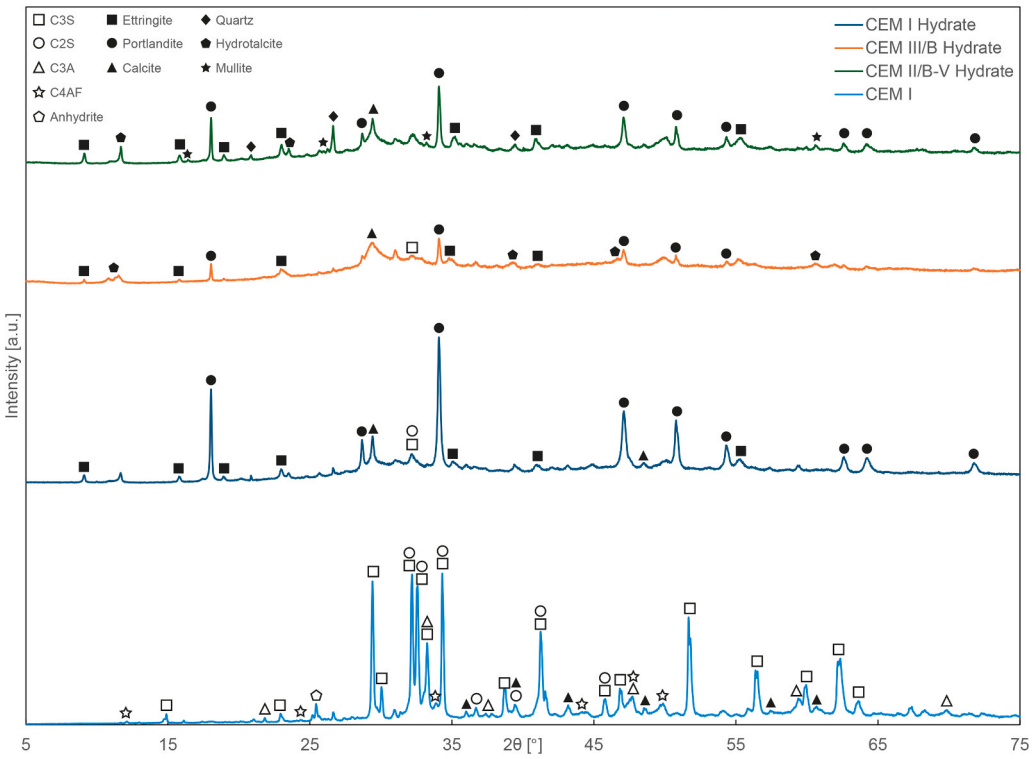

Fig. 9. X-Ray diffraction pattern of primary hydrated CEM I, CEM III/B, CEM II/B-V and unreacted CEM I. □ C3S (Alite; Ca_3SiO_5), ◯ C2S (Belite; Ca_2SiO_4), ΔC3A (Aluminate phase; $Ca_3Al_2O_6$), ☆C4AF (Ferrite phase; Ca_2AlFeO_5), ⌓Anhydrite ($CaSO_4$), ■ Ettringite ($Ca_6Al_2(SO_4)_3(OH)_{12}{\cdot}26\ H_2O$), ● Portlandite ($Ca(OH)_2$), ▲ Calcite ($CaCO_3$), ◆ Quartz ($SiO_2$), ★ Hydrotalcite ($Mg_6Al_2(OH)_{16}CO_3{\cdot}4\ H_2O$), ★ Mullite ($Al_6Si_2O_{13}$).

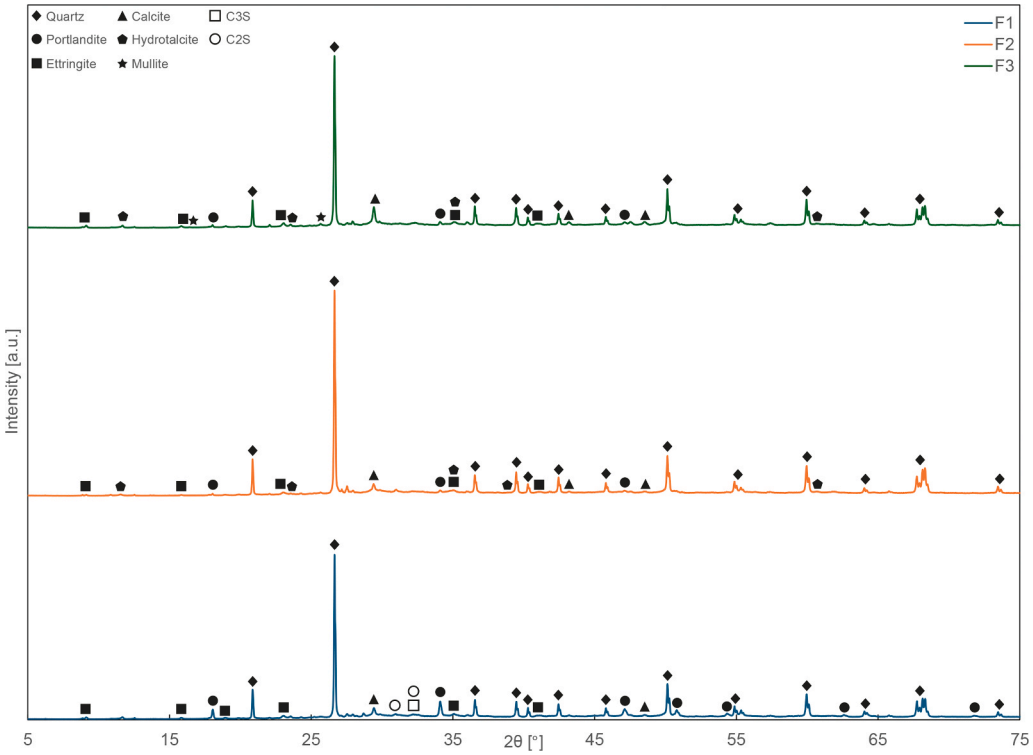

Fig. 10. X-Ray diffraction pattern of the residual cementitious fines F1, F2 and F3. ◆Quartz (SiO_2), ● Portlandite ($Ca(OH)_2$), ■ Ettringite ($Ca_6Al_2(SO_4)_3(OH)_{12}{\cdot}26\ H_2O$), ▲ Calcite ($CaCO_3$), ⌓ Hydrotalcite ($Mg_6Al_2(OH)_{16}CO_3{\cdot}4\ H_2O$), ★ Mullite ($Al_6Si_2O_{13}$), □ C3S (Alite; Ca_3SiO_5), ◯ C2S (Belite; Ca_2SiO_4).

for CEM I hydrate (4.03%), followed by CEM II/B-V hydrate (1.54%) and CEM III/B hydrate (0.78%). In the range 700–900 °C a comparable trend can be observed. Of the RCF samples (Fig. 15), F1 (CEM I based) has the highest weight loss related to portlandite. F2 (CEM III/B based) and F3 are more comparable, with F3 (CEM II/B-V) having a slightly higher weight loss. Unlike the hydrated reference cement types, a higher

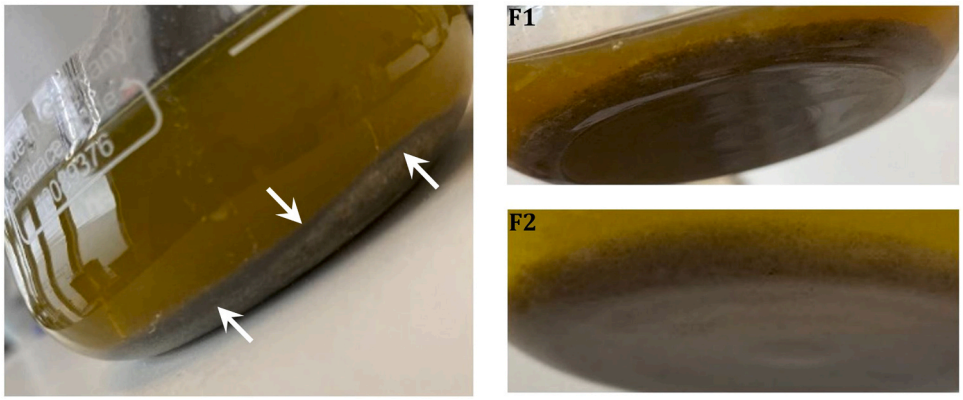

Fig. 11. Occurrence of a black layer (left, white arrows) for RCF sample F3 (CEM II/B-V based) indicating the presence of fly ash in the binder, while no black layer occurred (right) in RCF samples F1 and F2.

Fig. 12. Material of the black layer on a magnet, showing that the material consists of powders with magnetic properties.

Table 5
Estimated average sand content of the RCF samples F1 and F2, both not containing fly ash.

Type	Initial [g]	After washing [g]	+ /-	Estimated sand content [%]	+ /-	Amount for titration [g]	+ /-
F1	20.0	4.8	0.1	24.0	0.5	210.5	1.39
F2	20.0	4.7	0.1	23.5	0.5	209.2	1.37

decomposition of calcite was observed for F3, whereas the weight loss of F1 and F2 is more comparable.

Table 7 shows an overview of the weight losses due to H_2O and CO_2 evaporation and their corresponding portlandite and calcite content.

Table 6
The average starting pH and amount of 2 M HCl added to keep the pH below 7 for more than one hour. F1 showed a higher starting pH and amount of added HCl compared to F2.

Type	Start pH	+ /-	2 M HCl [ml]	+ /-
F1	11.12	0.25	1.07	0.12
F2	10.17	0.12	0.77	0.05

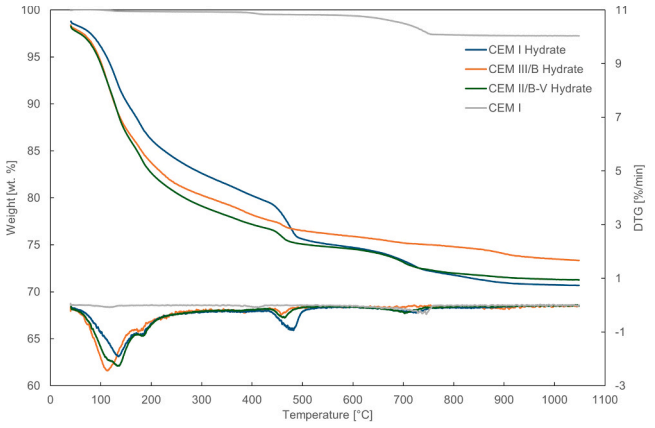

Fig. 14. TGA and DTG curves of primary hydrated CEM I, CEM III/B, CEM II/B-V and non-hydrated CEM I.

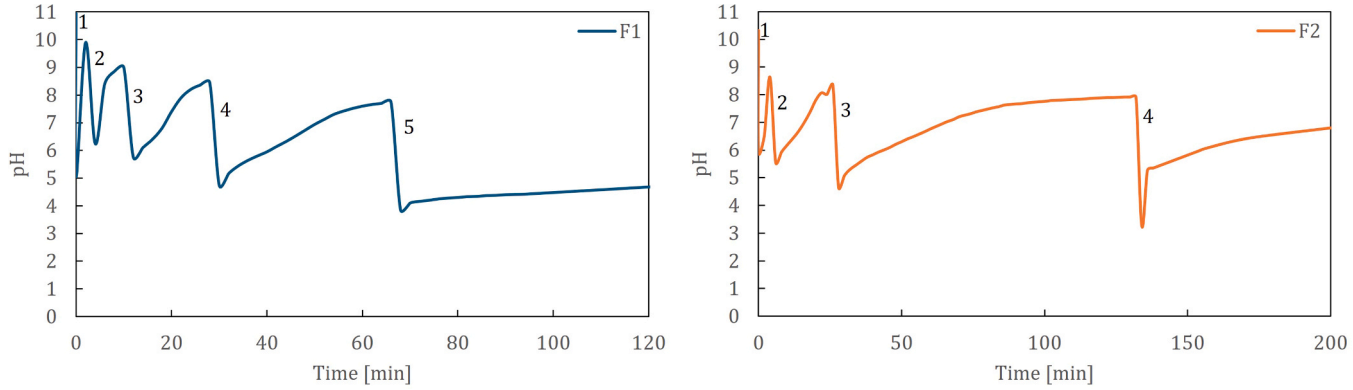

Fig. 13. Change in pH after adding HCl for Fines 1 (left) and Fines 2 (right). No 2 M HCl was added if the pH did not increase above 7 after 1 h.

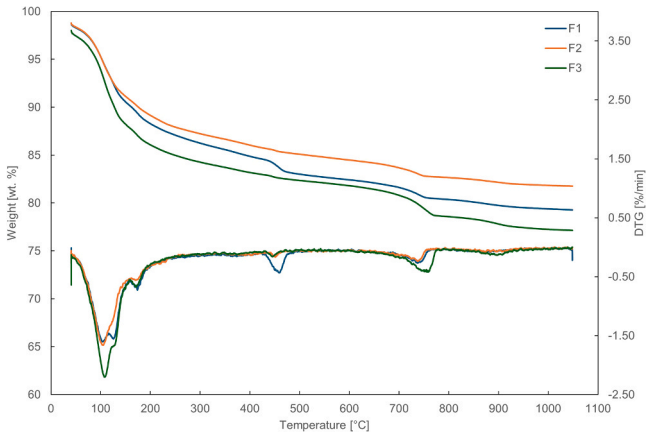

Fig. 15. TGA and DTG curves of the residual cementitious fines F1, F2 and F3.

The reference cements show a difference in both portlandite and calcite content. CEM I hydrate has the highest portlandite content, followed by CEM II/B-V hydrate and the lowest content can be observed for CEM III/B hydrate. A comparable trend can be observed for the calcite content. For the RCF samples, F1 (CEM I based) has the highest portlandite content, which is in agreement with the observations of the hydrates. The portlandite content of F2 (CEM III/B based) and F3 (CEM II/B-V based) are more comparable, with F3 having a slightly higher amount. The calcite content of the RCF samples, however, does not show a similar trend as those of the reference cement samples. Here, F3 has the highest calcite content, whereas F1 and F2 show a lower and comparable amount.

The DSC curves of both the reference cement- and the RCF samples are shown in Fig. 16. Comparing these results to Figs. 14 and 15 show that the thermal transitions occur at similar temperatures. Endothermic peaks can be observed in three temperature ranges, namely 40–250 °C, 400–550 °C and 700–900 °C, which correspond to the DTG peaks. A difference is observed in the DSC curve of the RCF samples. A small endothermic peak is present around 570 °C as a result of the transformation of α-quartz to β-quartz. This is an immediate but reversible transformation and does not result in a weight loss, but in a decrease in density (2.65 g/cm^3 to 2.53 g/cm^3) [20].

3.6. Fourier transform infrared spectroscopy

The FTIR spectra of the reference CEM I and hydrated cement CEM I, CEM III/B and CEM II/B-V and the RCF sampels are shown in Figs. 17 and 18. A clear distinction can be made between the non-hydrated CEM I and the three hydrated cement types. The main phases present in non-hydrated CEM I occur between 400 and 2100 cm^{-1} [48]. As a result of the hydration the absorbance bands in that region shift, occurring around 1100–1150 and 925 cm^{-1}. In the region 3000–4000 cm^{-1} absorbance bands appear due to water bonding and depending on the cement type the formation of portlandite (Fig. 17) [49,50]. For the CEM I hydrated samples a sharp peak related to portlandite can be distinguished around 3640 cm^{-1} [49–51]. This peak is not observed for the other two cement type hydrates. Other differences can be observed around 470–650 and 1100 cm^{-1} due to variations in sulfate and alumina containing phases [52]. These differences become more clear when taking the first derivative of the spectra (Fig. 19).

For the RCF samples (Fig. 18) the FTIR spectra appear comparable. Therefore, the first derivative was taken to better show variations within the curves (Fig. 20). The first derivative emphasizes rate of change in absorbance, effectively highlighting inflection points and resolving overlapping bands. This transformation is particularly valuable for cementitious materials, where complex mixtures can produce broad, overlapping absorbance features. As with the hydrated reference cement types, variations in the curves are observed between 470 and 1100 cm^{-1}. Especially within 550–650 cm^{-1} and around 1000 cm^{-1} differences in the peak appearance can be distinguished. Around 960 cm^{-1} a shift in the peak of the F2 sample (CEM III/B based) occurs.

Table 7
Amount of H_2O and CO_2 and their corresponding portlandite ($Ca(OH)_2$) and calcite ($CaCO_3$) content.

Content [wt%]	H_2O in $Ca(OH)_2$	CO_2 in $CaCO_3$	$Ca(OH)_2$	$CaCO_3$	Total
F1	1.41	1.22	5.80	2.77	19.44
F2	0.29	1.20	1.19	2.73	17.03
F3	0.36	2.66	1.48	6.05	20.87
CEM I hydrate	4.03	2.18	16.57	4.95	28.12
CEM III/B hydrate	0.78	0.72	3.21	1.64	25.06
CEM II/B-V hydrate	1.54	1.55	6.33	3.52	27.00
CEM I	0.20	2.06	0.82	4.68	2.76

3.7. Polarized and fluorescence microscopy of thin sections

Fig. 21 shows microscopic images of thin sections taken from the three concrete blocks. Based on these images a clear distinction can be made regarding present binder types. In the thin sections of block 2 (CEM III/B based) the presence of ground granulated blast furnace slag (GGBS) was observed, whereas block 3 (CEM II/B-V based) contains spherical fly ash (FA) particles. Analysis of the thin sections of block 1 (CEM I based) showed Portland cement as the main binder, but a minor amount of fly ash was also observed. This amount was substantially lower compared to that of block 3. Besides identification of the binder type, non-hydrated cement particles, unreacted GGBS and FA particles were also observed.

Visual inspection of freshly drilled cores can also give a starting indication regarding the used cement type within the concrete. Especially, concrete containing CEM III/B can be recognized by its darker blueish color (Fig. 22). Between CEM I and CEM II/B-V this is more difficult, because their color is comparable. However, CEM II/B-V is slightly darker compared to CEM I.

4. Discussion

This research examined residual cementitious fines (RCF) derived from three different concrete types with known composition, differing solely in the cement type used. The investigation assessed the feasibility of several available analytical methods for determining the cement types in these RCF samples. Furthermore, the application potential of these methods for adaptation to non-destructive binder characterization in EoL concrete was evaluated.

4.1. Identification characteristics

Based on various properties, a clear distinction can be made between the types of cement present in RCF examined in this study. Fig. 6 shows that the chemical composition as examined by HXRF differs for several elements and that these can be used as tracers. In particular, the contents of CaO, Al_2O_3, Fe_2O_3 and MgO are discriminative. RCF F2 (CEM III/B based) is recognized by a higher amount of Al_2O_3 in combination with a higher MgO content, whereas for the identification of RCF F3 (CEM II/B-V based) the higher Al_2O_3 content is combined with a larger amount of Fe_2O_3. These observations align with values reported in the literature [13,53–56]. However, residual sand in the RCF can affect elemental concentrations, complicating the establishment of absolute threshold values. Reliable thresholds require consistent recycling processes yielding fines of homogenous composition, as varying sand content from different methods would alter these values. Since river sand mainly consists of SiO_2 [13,57,58], using ratios based on tracer elements other

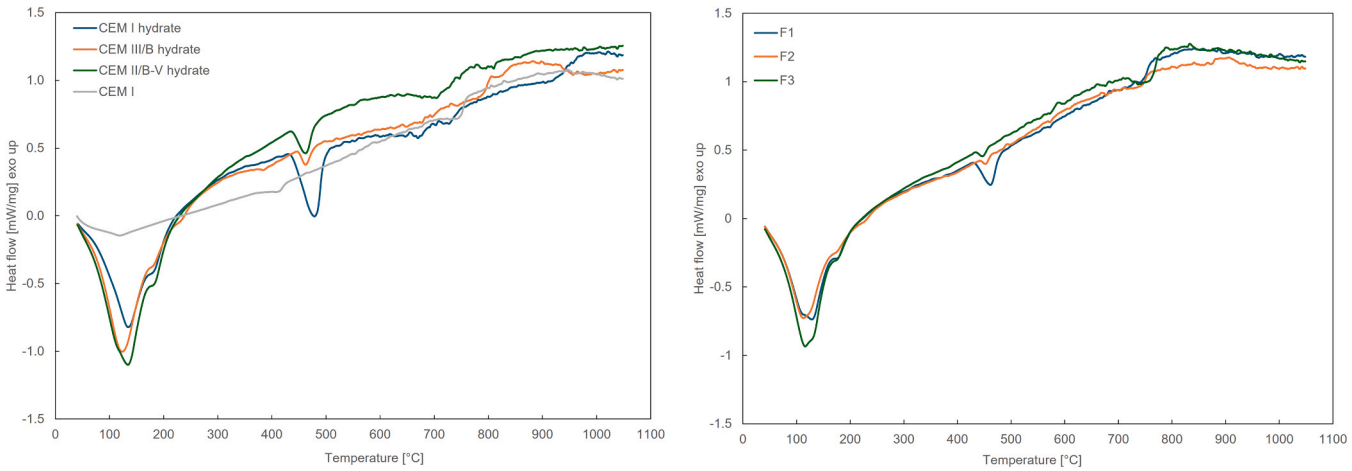

Fig. 16. DSC curves of the reference cements (left) and residual cementitious fines (right).

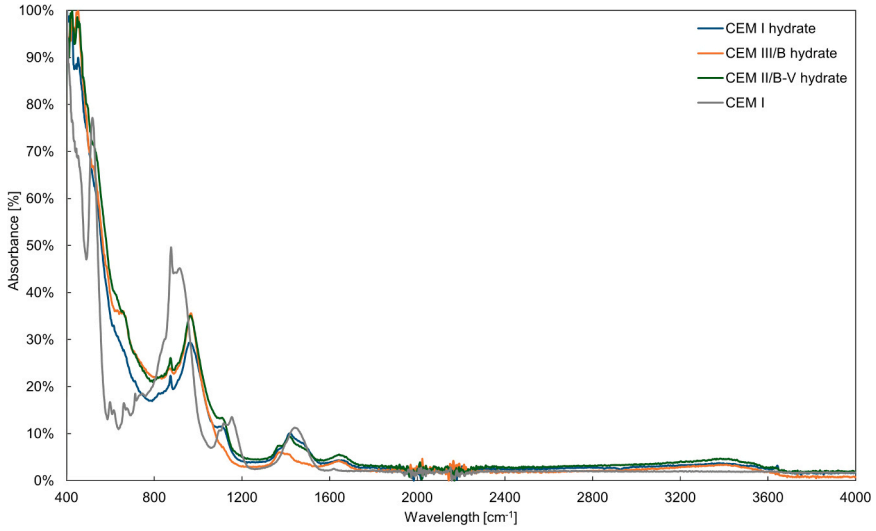

Fig. 17. Normalized FTIR curves of primary hydrated CEM I, CEM III/B, CEM II/B-V and unreacted CEM I.

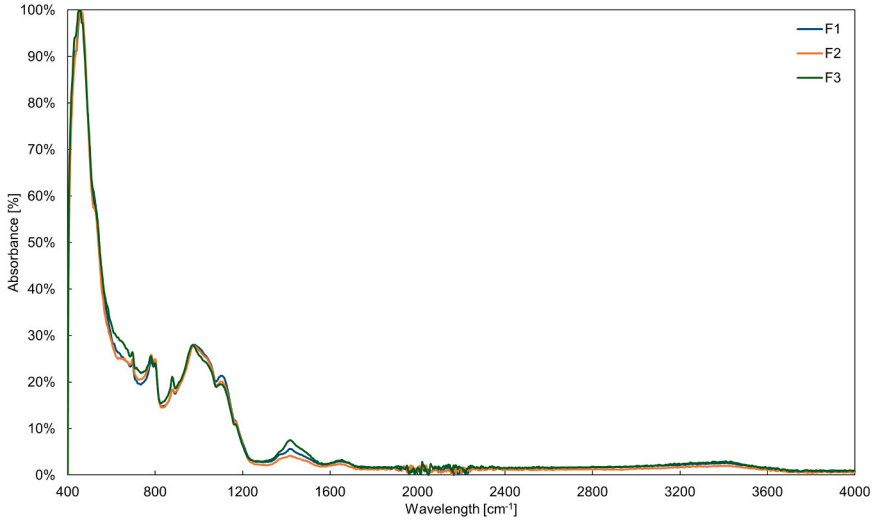

Fig. 18. Normalized FTIR curves of the residual cementitious fines F1, F2 and F3.

than SiO_2 improves distinction between cement types (Table 8). RCF differences also appear in the mineralogical compositions as determined

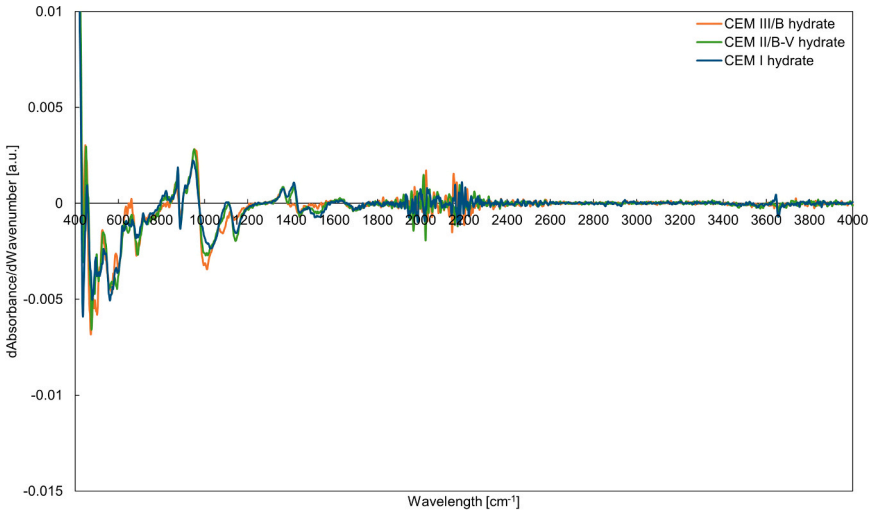

Fig. 19. First derivative of the FTIR spectra of the primary hydrated cement types.

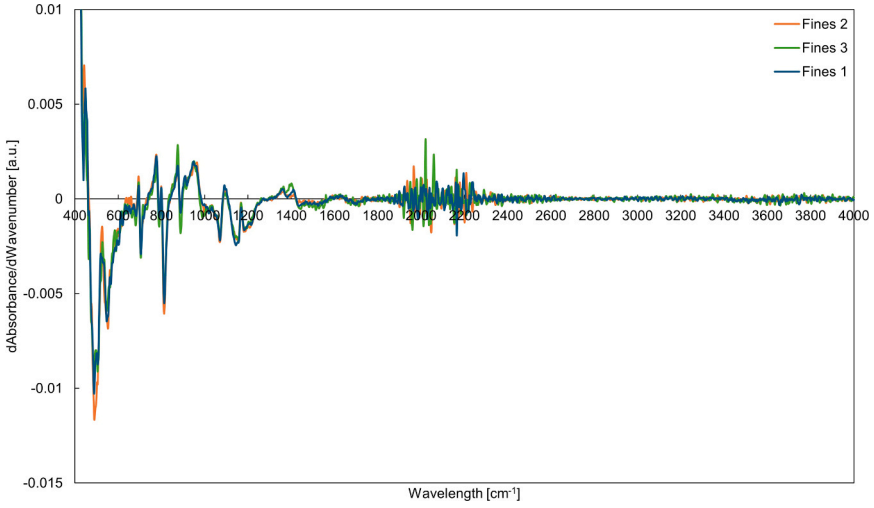

Fig. 20. First derivative of the FTIR spectra of the residual cementitious fines.

by XRD, where specific crystalline phases can be used for identification. In particular, mullite, hydrotalcite, and portlandite are of interest. Since both CEM III/B and CEM II/B-V are a combination of CEM I with blast furnace slag and fly ash, respectively, there is a significant overlap in the phases that are formed. However, RCF F2 (CEM III/B based) is identifiable by hydrotalcite presence, and RCF F3 (CEM II/B-V based) by the presence of mullite [54,59]. Additionally, differences can be seen in the relative portlandite mineral content [16], which are highest in RCF F1 (CEM I based), followed by RCF F3 and RCF F2. The reason for this is that both GGBS and FA consume portlandite during hydration [60,61]. This pattern is also observed in the titration results (shown in Table 6) distinguishing RCF F1 from RCF F2: due to portlandite consumption by GGBS, RCF F2 requires less HCl to maintain a pH below 7 for over an hour. RCF F3 is uniquely identified by a persistent black layer after selective dissolution. The material of this black layer has magnetic properties (Fig. 12), suggesting that it contains iron-bearing phases, such as magnetite and maghemite [62,63].

The higher amount of portlandite in RCF F1 is also evident from the results obtained with TGA and DSC analysis. This amount is approximately 3.9 and 4.9 times greater than that of RCF F3 and RCF F2, respectively. The difference between RCF F2 and RCF F3 is smaller, with RCF F3 having a slightly higher portlandite content. The calcite content, however, is highest for RCF F3. Reason for this can be the higher specific surface area, which may influence the carbonation rate during storage. Based on the CO_2 amount related to calcite, it may be possible to determine the initial amount of portlandite present before carbonation occurs. If it is assumed that the estimated CO_2 content was fully bound as calcite by the reaction with portlandite, it can be recalculated using formulas 6–8.

$$Ca(OH)_2 + CO_2 \rightarrow CaCO_3 + H_2O \tag{6}$$

$$m_{CH} = m_{\overline{C}} \times \frac{74\frac{g}{mol}}{44\frac{g}{mol}} \tag{7}$$

$$CH_{total} = CH_{CO_2} + CH_{H_2O} \tag{8}$$

The total amount of portlandite based on these calculations is shown in Table 8. From the hydrated references cements CEM I hydrate would have had the highest total portlandite content, followed by CEM II/B-V hydrate and CEM III/B hydrate, which is in agreement with the order observed for the measured portlandite content shown in Table 7. For the RCF samples a similar trend as for the reference hydrates can be observed. The difference between RCF F2 (CEM III/B based) and F3 (CEM II/B-V based) becomes more distinct with this approach, showing a higher total portlandite content for RCF F3 than for RCF F2. These

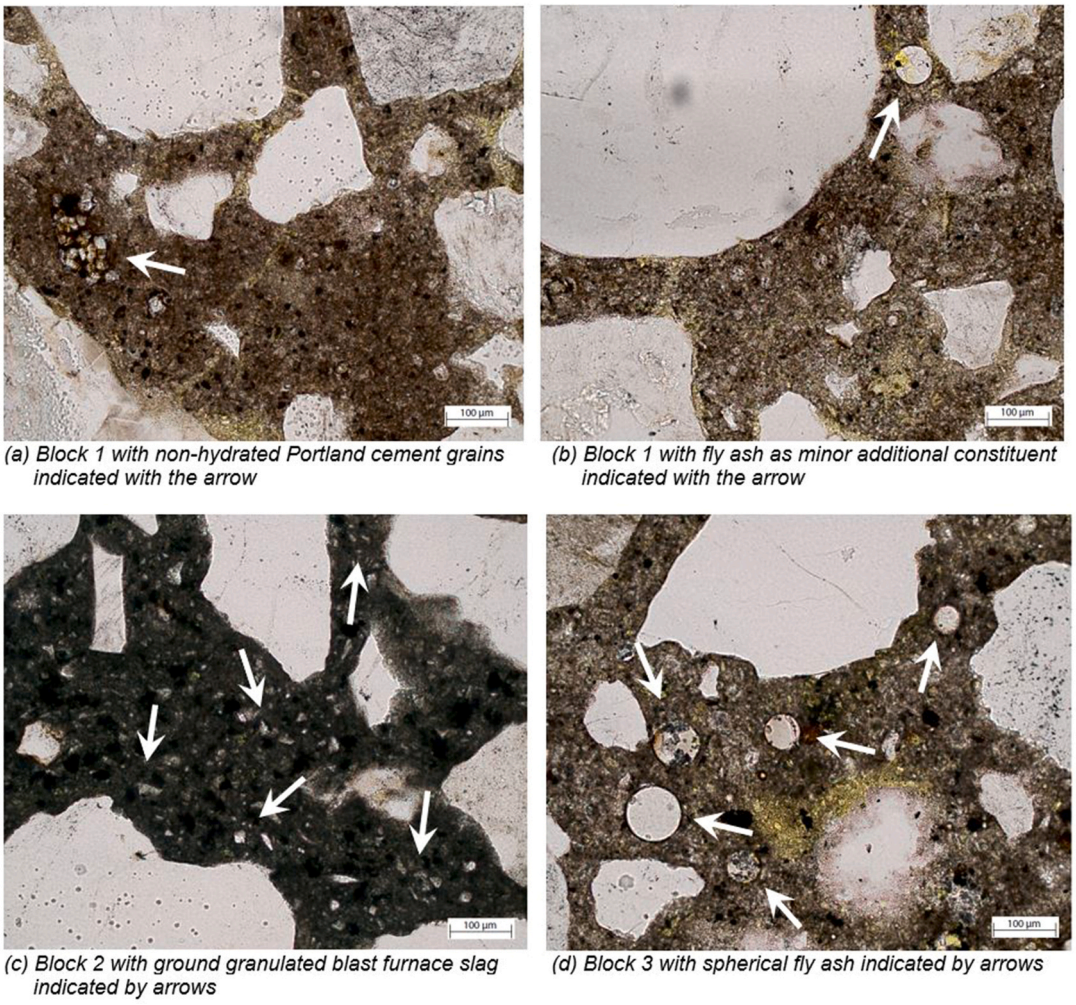

Fig. 21. Microscopic images of (a) Block 1 containing CEM I, (b) Block 2 containing CEM III/B and (c) Block 3 containing CEM II/B-V in plane polarized light. Unreacted Portland cement, ground granulated blast furnace slag and fly ash particles can be distinguished.

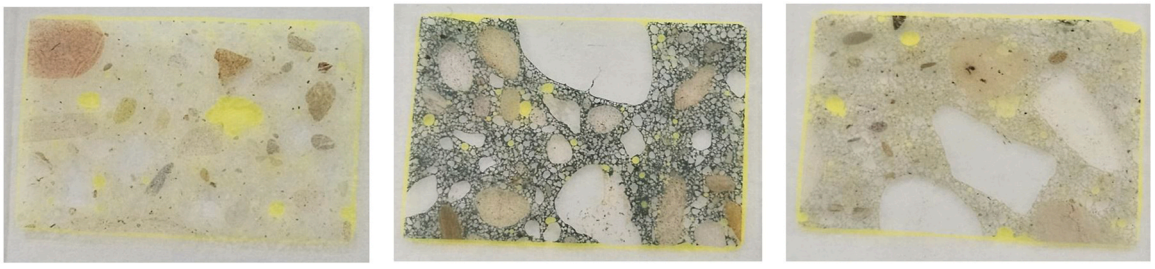

Fig. 22. Thin sections of concrete cores (non-carbonated) of block 1, block 2 and block 3. Block 2 has a distinct darker blue color compared to the other two blocks, indicating the presence of a slag containing cement type such as CEM III/B.

portlandite trends also align with the XRD results. However, portlandite is not the only component in cement that carbonates. Other components, such as C-S-H, ettringite, and unreacted particles, can all react with CO_2 and contribute to the amount of calcite measured [64,65]. Therefore, the value shown in Table 8 may be an overestimation of the actual value. Nevertheless, this approach may result in an identification of the cement type. Portlandite is the component that contributes the most to the carbonation reaction, until depletion after which the carbonation reaction mainly shifts to other components [26,66,67]. Based on the TGA results, a significant amount of portlandite still remains in the samples, which leads to the assumption that other components have limited contribution to the carbonation and that the measured CO_2 could be

Table 8
Estimation of the total amount of portlandite present based on the combination of the amount of CO_2 in calcite and the amount of portlandite from Table 7.

	CO2 in CC^{-}	CH		CH total
		Based on CO_2	Based on H_2O	
F1	1.22	2.05	5.80	7.85
F2	1.2	2.02	1.19	3.21
F3	2.66	4.47	1.48	5.95
CEM I hydrate	2.18	3.67	16.57	20.23
CEM III/B hydrate	0.72	1.21	3.21	4.42
CEM II/B-V hydrate	1.55	2.61	6.33	8.94

used to estimate the total portlandite content. Although carbonation alters calcium bearing phases, it does not compromise cement type identification in this study. The analytical techniques remain capable of distinguishing between cement types, as carbonation primarily affects surface zones while recycled concrete fines represent mechanically diluted and homogenized bulk material. Relative binder differences are preserved with representative sampling and proper storage. For on-site surface measurements, carbonation and efflorescence may locally mask diagnostic signals depending on the technique. This requires technique specific correction strategies.

The FTIR results show comparable curves for the three RCF samples. However, when taking the first derivative of these curves variations in the curves become more apparent, which may help discriminating between cement types. Tang et al. [18] also found that differences between concrete mixtures can be clarified by comparing the first derivatives of the FTIR spectra curves. Microscopic analysis of thin sections taken from concrete core samples clearly reveal the differences between the types of cement present. The angular, glassy slag and spherical fly ash particles result in the identification of the cement types present in the concrete cores [68]. Even though a small amount of fly ash could be observed in the thin section of block 1 (CEM I based), this amount was significantly lower than that of block 3 (CEM II/B-V based), which pointed towards fly ash being used as a minor additional constituent in the Portland cement used in block 1. An overview of the characteristics of interest for the identification of the cement type is shown in Table 9. It should be noted that the potential of the studied binder identification methods are specific to the RCF used in this research. In practice, moisture may lead to deviation in the measurements results. Nevertheless, this study showed that diagnostic chemical, mineralogical and thermal features remain sufficiently pronounced to allow reliable distinction between the different cement types. For concrete containing different aggregate types or mineral additions, the results may differ. For example, RCF derived from concrete made with limestone aggregates may exhibit different characteristics, and consequently, the determined identification characteristics may vary. Therefore, for other concrete compositions, these methods should be re-evaluated to assess the impact of compositional variations.

4.2. Potential of identification methods for practical settings

Various methods have been used to gain insight into the properties of the RCF samples studied and the associated identification of the type of cement present in these. The question is which of these methods have the highest potential for practical, non-destructive use in determining the type of cement before the demolition of a structure. Methods demonstrating potential require field validation to establish their identification characteristics under on-site conditions and to develop a standardized measurement protocol. Polarized and fluorescence microscopy of thin sections provides certainty when it comes to identifying the components in the concrete. However, this is a destructive method that requires drilling cores to make thin sections for microscopic analysis [69]. As a result, it is a time-consuming and expensive process. The HXRF, on the other hand, is a portable, non-destructive instrument with short measurement times [12]. This allows for rapid on-site determination, which is highly desirable in practice. This method shows great potential, which was also found by Nedeljković et al. [13]. Their study established that CaO, SiO_2, Al_2O_3, Fe_2O_3 and MgO can be used for identification with short measurement times (30 s minimum). However, they mentioned that concrete curing affects the results. Selective dissolution and titration of RCF derived from the concrete of interest is not preferred on site, because of the use of acid and the preference of a fine powder fraction during the titration measurements. A fine powder has a larger surface area, resulting in a higher amount of OH^- ions being leached into the solution [70,71]. Therefore, both selective dissolution and titration are of interest in a laboratory setting, but from a practical viewpoint not for on-site testing. The same may be true for the TGA and DSC. Both methods heat the samples over time to high temperatures (in this study 1050 °C). Depending on the heating rate, it can take time to obtain the measurement results. In this research, the measurement time was approximately 2 h without cooling. Additionally, both methods are destructive, as the high temperature treatment makes it impossible to measure the same area twice. For on-site measurements both the high temperatures and the long measurement time are not preferred, but it can still give valuable insight in the powder characteristics obtained after recycling when analysed in a laboratory setting. Both XRD and FTIR are already available as portable methods, but they have never been used before for the analysis of concrete prior to demolition. For XRD, a portable option is studied and used in for example soil research and planetary explorations (Mars missions). Often, it is still necessary to use a powder sample, after which the device can provide results within a few minutes [72,73]. It is possible to obtain a powder sample on-site, but this is less efficient than using a method that can perform measurements immediately. Further development of the portable XRD may make this possible in the future. In the art industry, for example, research is already being conducted on non-destructive portable XRD setups to prevent damage to the art [74,75]. These may also be of interest as a non-destructive method to analyse the binder type in EoL concrete. Portable FTIR is used in different industries, such as pharmaceuticals, forensic science, food, chemicals, cosmetics, and more [76]. Within the cement industry, FTIR is often used for insight in the formed hydration products, using chemical admixtures and cement constituents [77]. It has not been used as a method for the identification of the cement type within the concrete recycling industry. The ease in which this method is portable, is comparable to the HXRF. The question is to what extent identification in field applications will be possible. Overlapping peaks as a result of comparable chemical components will make this difficult [18,48,78]. Setting up a database with reference spectra may be needed for the approach of cement type identification [48]. An overview of the potential of the various methods is given in Table 10.

Table 9
Characteristics for the identification of the cement type in residual cementitious fines.

Method	F1 (CEM I)	F2 (CEM III/B)	F3 (CEM II/B-V)
HXRF	CaO $Fe_2O_3/CaO < 9$ $Al_2O_3/CaO < 18$	Al_2O_3, MgO $Fe_2O_3/Al_2O_3 < 40$	Al_2O_3, Fe_2O_3 $Fe_2O_3/CaO > 9$ $Al_2O_3/CaO > 18$
XRD	High portlandite peaks	Hydrotalcite	Mullite, hydrotalcite
Selective dissolution, titration	$\geq$ 1.0 ml 2 M HCl	< 0.8 ml 2 M HCl	Black layer
TGA, DSC	High portlandite content	Low portlandite content	Medium portlandite content
FTIR	550–650 cm^{-1}, 1000 cm^{-1}	550–650 cm^{-1}, 960 cm^{-1}, 1000 cm^{-1}	550–650 cm^{-1}, 1000 cm^{-1}
PFM	Portland cement, unhydrated cement particles	Angular, glassy GGBS particles	Spherical fly ash particles

5. Conclusions

This study demonstrates that multiple analytical methods can effectively characterize residual cementitious fines (RCF) and distinguish the cement types from which they originate, based on their chemical and mineralogical signatures. The results confirm the potential of these methods for cement identification and assess their suitability for further development into non-destructive identification techniques applicable to End-of-Life (EoL) concrete. Accurate identification of the cement type is crucial, as it directly influences the quality, processing strategy and reuse potential of RCF in new (concrete) applications. The

Table 10
Potential of the studied methods for practical applications and on-site testing.

Method	Potential	Remarks
HXRF	High	Fast, on-site identification.
XRD	High	Often requires powder samples. However, non-invasive options developing in other industries.
Selective dissolution, titration	Low	Destructive. Use of acid not preferred on-site. Titration prefers powders for analysis.
TGA, DSC	Low	Destructive, time consuming. Possibly difficult to develop as a portable method.
FTIR	Medium	Fast, first derivative required. Overlapping peaks may make identification difficult.
PFM	High	Destructive. Takes time to prepare thin sections. Good distinction cement types.

following key conclusions can be drawn:

- Distinct cement identification is achievable: The three investigated cement types (CEM I, CEM III/B, and CEM II/B-V) were reliably differentiated across all tested methods. Consistent variations in chemical (e.g., CaO, Al_2O_3, Fe_2O_3, MgO) and mineralogical markers (e.g., portlandite, hydrotalcite, mullite) were observed between samples. Quantitatively, HXRF results deviated by less than ±5.5% from stationary XRF analyses, confirming its reliability for compositional discrimination.
- Handheld X-ray fluorescence (HXRF) holds the highest practical potential: HXRF provided rapid, non-destructive and reproducible on-site identification of cement types through characteristic oxide ratios (e.g. Fe_2O_3/Al_2O_3, Fe_2O_3/CaO and Al_2O_3/CaO). Its ability to deliver results within seconds makes it particularly suited for pre-demolition screening. In contrast, methods such as XRD, FTIR, TGA/DSC, and titration currently require laboratory conditions or destructive sampling, which limits their immediate field applicability.
- Residual cementitious fines mirror the properties of their corresponding reference cements: The main difference lies in the presence of quartz derived from siliceous aggregates in the RCF fractions. This consistency indicates that the crushing and separation process preserves the key cement characteristics necessary for reliable identification and subsequent reuse potential assessment.
- Broader sustainability impact: Accurate in-situ binder identification enables source separation of EoL concrete before crushing, leading to more homogeneous and higher-quality RCF fractions. This targeted approach enhances opportunities for clinker substitution in new concrete mixtures and contributes directly to reducing the carbon footprint of concrete production in alignment with circular economy goals.

Further work should focus on (i) developing calibration and reference databases for HXRF-based cement identification, (ii) validating the proposed method across diverse concrete structures of different ages, (iii) expanding the method to include additional cement types, particularly cement types containing limestone, which is gaining market share in Europe, and (iv) exploring portable FTIR and emerging non-invasive XRD technologies for complementary on-site characterization. Pursuing these directions is driven by the sustainability potential and industrial relevance, as scalable in-situ cement identification would enable higher-quality RCF fractions, increase opportunities for clinker substitution, and contribute to reducing the carbon footprint of concrete production in alignment with circular economy goals and broader industrial adoption. Integration of such techniques could significantly improve circularity in the concrete value chain.

Declaration of Competing Interest

The authors declare that they have no known competing financial interests or personal relationships that could have appeared to influence the work reported in this paper.

Acknowledgments

The authors like to thank Urban Mine B.V. for funding this research.

Appendix A – Comparison of trend between the handheld XRF and the desktop XRF

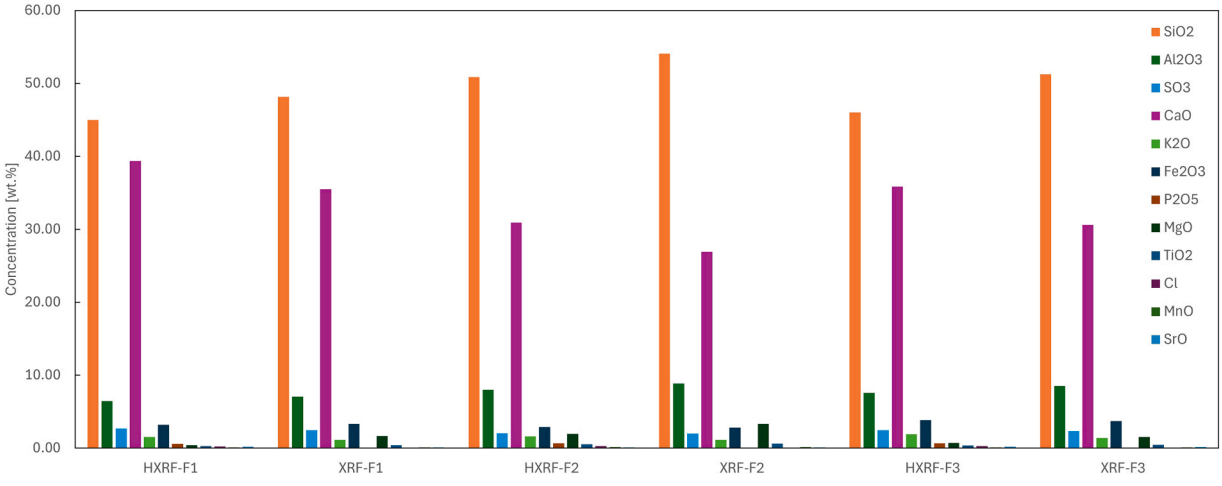

Figure 23. Handheld and desktop XRF measurements of the residual cementitious fines F1 (HXRF-F1; XRF-F1), F2 (HXRF-F2; XRF-F2) and F3 (HXRF-F3; XRF-F3). Comparable trends are observed between the handheld and desktop measurements

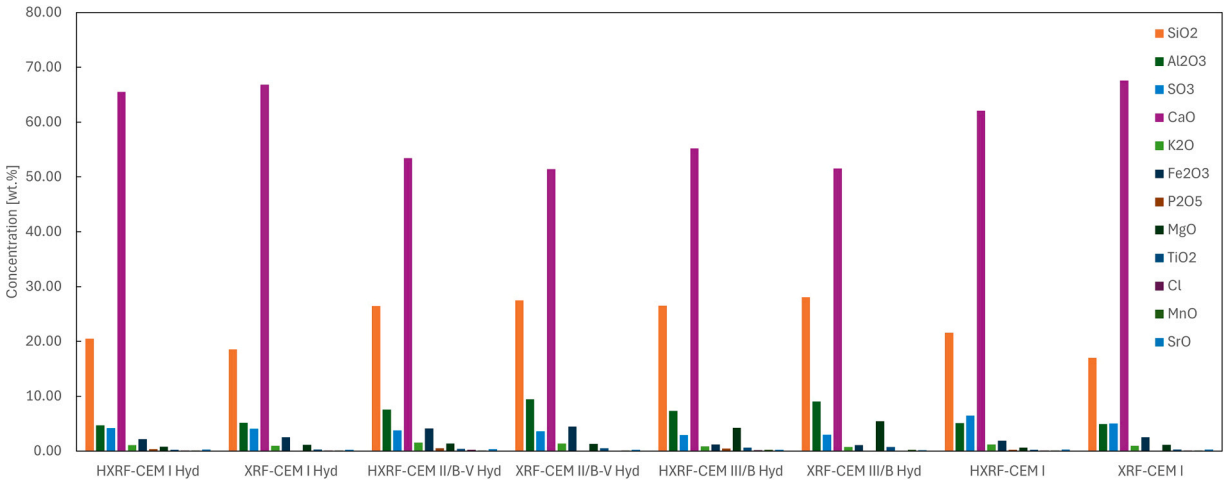

Figure 24. Handheld and desktop XRF measurements of the reference binders CEM I hydrate, CEM II/B-V hydrate, CEM III/B hydrate and CEM I. Comparable trends are observed between the handheld and desktop measurements

Data availability

Data will be made available on request.

References

[1] E. Benhelal, G. Zahedi, E. Shamsaei, A. Bahadori, Global strategies and potentials to curb CO2 emissions in cement industry, J. Clean. Prod. 51 (2013) 142–161, https://doi.org/10.1016/j.jclepro.2012.10.049.

[2] S.A. Miller, F.C. Moore, Climate and health damages from global concrete production, Nat. Clim. Change (2020) 1–5, https://doi.org/10.1038/s41558-020-0733-0.

[3] H. Mehdizadeh, X. Cheng, K.H. Mo, T.-C. Ling, Upcycling of waste hydrated cement paste containing high-volume supplementary cementitious materials via CO2 pre-treatment, J. Build. Eng. 52 (2022) 104396, https://doi.org/10.1016/j.jobe.2022.104396.

[4] A.T.M. Alberda van Ekenstein, H.M. Jonkers, M. Ottelé, Downstream processing of end-of-life concrete for the recovery of high-quality cementitious fractions, Cement 18 (2024) 100121, https://doi.org/10.1016/j.cement.2024.100121.

[5] Nederlands Normalisatie-instituut, NEN-EN 197-1 Cement. Part 1: Composition, Specifications and Conformity Criteria for Common Cements, CEN Brussels, Belgium, 2011.

[6] Betonhuis. (n.d.). Cement en Bindmiddelen. Retrieved from ⟨https://betonhuis.nl/betonhuis/cement-en-bindmiddelen#:~:text=In%20Nederland%20worden%20drie%20soorten,dat%20het%20vrij%20snel%20uithardt⟩.

[7] C.J.W.P. Groot, P. Bartos, J.J. Hughes, Historic mortars: characteristics and tests-Concluding summary and state of the art. Paper presented at the Proc. Intern RILEM workshop, Advanced Concrete and Masonry Centre, 1999.

[8] J.J. Hughes, J. Válek, C.J.W.P. Groot, 2018. Historic mortars: advances in research and practical conservation. doi:https://doi.org/10.1007/978-3-319-91606-4.

[9] T.G. Nijland, J.A. Larbi, Microscopic examination of deteriorated concrete. Non-Destructive Evaluation of Reinforced Concrete Structurespp, Elsevier, 2010, pp. 137–179.

[10] W.J. French, Concrete petrography: a review, Q. J. Eng. Geol. Hydrogeol. 24 (1) (1991) 17–48, https://doi.org/10.1144/GSL.QJEG.1991.024.01.0.

[11] D. JanaSample preparation techniques in petrographic examinations of construction materials: a state-of-the-art review. Paper presented at the Proceedings of the twenty-eighth Conference on Cement Microscopy2006.

[12] I. Liritzis, N. ZachariasPortable XRF of archaeological artifacts: current research, potentials and limitations. X-ray fluorescence spectrometry (XRF) in geoarchaeology, pp. 109-142.2011.

[13] M. Nedeljković, N. Tošić, P. Holthuizen, F. França de Mendonça Filho, O. Çopuroğlu, E. Schlangen, S. Fennis, Non-destructive screening methodology based on handheld XRF for the classification of concrete: cement type-driven separation, Mater. Struct. 56 (3) (2023) 54, https://doi.org/10.1617/s11527-023-02147-3.

[14] A.W. Coats, J.P. Redfern, Thermogravimetric analysis. A review, Analyst 88 (1053) (1963) 906–924, https://doi.org/10.1039/AN9638800906.

[15] J. Elsen, Microscopy of historic mortars—a review, Cem. Concr. Res. 36 (8) (2006) 1416–1424, https://doi.org/10.1016/j.cemconres.2005.12.006.

[16] B. Middendorf, J.J. Hughes, K. Callebaut, G. Baronio, I. Papayianni, Investigative methods for the characterisation of historic mortars—part 1: mineralogical characterisation, Mater. Struct. 38 (8) (2005) 761–769, https://doi.org/10.1007/BF02479289.

[17] PerkinElmer, 2013, Differential Scanning Calorimeter (DSC), A beginner's guide.

[18] P.L. Tang, M. Alqassim, N.N. Daéid, L. Berlouis, J. Seelenbinder, Nondestructive handheld fourier transform infrared (FT-IR) analysis of spectroscopic changes and multivariate modeling of thermally degraded plain portland cement concrete and its slag and fly ash-based analogs, Appl. Spectrosc. 70 (5) (2016) 923–931, https://doi.org/10.1177/0003702816638306.

[19] H.F.W. Taylor. Cement Chemistry, 2 ed., Thomas Telford London, 1997.

[20] M.V.A. Florea, Z. Ning, H.J.H. Brouwers, Activation of liberated concrete fines and their application in mortars, Constr. Build. Mater. 50 (2014) 1–12, https://doi.org/10.1016/j.conbuildmat.2013.09.012.

[21] E. Kwon, J. Ahn, B. Cho, D. Park, A study on development of recycled cement made from waste cementitious powder, Constr. Build. Mater. 83 (2015) 174–180, https://doi.org/10.1016/j.conbuildmat.2015.02.086.

[22] L. Oksri-Nelfia, P.-Y. Mahieux, O. Amiri, P. Turcry, J. Lux, Reuse of recycled crushed concrete fines as mineral addition in cementitious materials, Mater. Struct. 49 (8) (2016) 3239–3251, https://doi.org/10.1617/s11527-015-0716-1.

[23] L. Zhang, Y. Ji, G. Huang, J. Li, Y. Hu, Modification and enhancement of mechanical properties of dehydrated cement paste using ground granulated blast-furnace slag, Constr. Build. Mater. 164 (2018) 525–534.

[24] J. Topič, Z. Prošek, Properties and microstructure of cement paste including recycled concrete powder, Acta Polytech. 57 (1) (2017) 49–57.

[25] A. Carriço, J.A. Bogas, M. Guedes, Thermoactivated cementitious materials–a review, Constr. Build. Mater. 250 (2020) 118873, https://doi.org/10.1016/j.conbuildmat.2020.118873.

[26] M. Zajac, J. Skibsted, P. Durdzinski, F. Bullerjahn, J. Skocek, M.B. Haha, Kinetics of enforced carbonation of cement paste, Cem. Concr. Res. 131 (2020) 106013, https://doi.org/10.1016/j.cemconres.2020.106013.

[27] Z. Shui, D. Xuan, W. Chen, R. Yu, R. Zhang, Cementitious characteristics of hydrated cement paste subjected to various dehydration temperatures, Constr. Build. Mater. 23 (1) (2009) 531–537.

[28] S.S. Trivedi, F. Ansari, B.B. Das, S. Barbhuiya, Effect of CO2 curing on phase compositions of nano silica blended cementitious mortar partially replaced with carbonated recycled fine aggregates, Constr. Build. Mater. 491 (2025) 142789.

[29] Nederlands Normalisatie-instituut, NEN-EN 197-6 Cement - Part 6: Cement with Recycled Building Materials, CEN Brussels, Belgium, 2023.

[30] L. Bertolini, F. Lollini, Effects of weathering on colour of concrete paving blocks, Eur. J. Environ. Civ. Eng. 15 (6) (2011) 939–957.

[31] L. Ge, W. Lai, Y. Lin, Influence of and correction for moisture in rocks, soils and sediments on in situ XRF analysis, X-Ray Spectrom. Int. J. 34 (1) (2005) 28–34.

[32] A.R. Schneider, B. Cancès, C. Breton, M. Ponthieu, X. Morvan, A. Conreux, B. Marin, Comparison of field portable XRF and aqua regia/ICPAES soil analysis and evaluation of soil moisture influence on FPXRF results, J. Soils Sediment. 16 (2016) 438–448.

[33] M.V.A. Florea, H.J.H. Brouwers, Properties of various size fractions of crushed concrete related to process conditions and re-use, Cem. Concr. Res. 52 (2013) 11–21, https://doi.org/10.1016/j.cemconres.2013.05.005.

[34] S.S. Trivedi, F. Ansari, P.K.K. Goud, S. Joy, B. Das, S. Barbhuiya, Carbon capture efficiency of ultrafine cementitious substituents and fine aggregate alternatives subjected to accelerated CO2 curing, J. Build. Eng. 99 (2025) 111655.

[35] Rutte Groep (Producer). 2019. How does the SmartLiberator work? [Video file] Retrieved from ⟨https://www.youtube.com/watch?v=upfKRuKFUiQ⟩.

[36] Schenk, K.J. 2011. The Netherlands Patent No.

[37] Nederlands Normalisatie-instituut. 2008. NEN-EN 1097-5: Test for mechanical and physical properties of aggregates - Part 5: Determination of the water content by drying in a ventilated oven. Belgium: CEN Brussels.

[38] A. Alberda van Ekenstein, H. Jonkers, M. Ottelé, Characterizing cement types in end-of-life concrete: a practical approach using handheld X-ray fluorescence,

Constr. Build. Mater. 502 (2025) 144293, https://doi.org/10.1016/j.conbuildmat.2025.144293.
[39] Nederlands Normalisatie-instituut, NEN-EN 196-2 Method of Testing Cement - Part 2: Chemical analysis of Cement, CEN Brussels, Belgium, 2013.
[40] Y. Li, H. Lin, Z. Wang, Quantitative analysis of fly ash in hardened cement paste, Constr. Build. Mater. 153 (2017) 139–145, https://doi.org/10.1016/j.conbuildmat.2017.07.106.
[41] S.S. Trivedi, B.B. Das, S. Barbhuiya, Performance of construction and demolition waste as recycled aggregates in concrete–review, Proc. Inst. Civ. Eng. -Constr. Mater. 178 (1) (2025) 20–47.
[42] S.S. Trivedi, D. Sarangi, B. Das, S. Barbhuiya, Influence of multi-stage processing and mechano-chemical treatments on the hydration and microstructure properties of recycled aggregate concrete, Constr. Build. Mater. 409 (2023) 133993.
[43] L. Alarcon-Ruiz, G. Platret, E. Massieu, A. Ehrlacher, The use of thermal analysis in assessing the effect of temperature on a cement paste, Cem. Concr. Res. 35 (3) (2005) 609–613.
[44] J.A. Bogas, A. Carrico, A.J. Tenza-Abril, Microstructure of thermoactivated recycled cement pastes, Cem. Concr. Res. 138 (2020) 106226.
[45] I. Hager, Behaviour of cement concrete at high temperature, Bull. Pol. Acad. Sci. Tech. Sci. 1 (2013).
[46] C. Alonso, L. Fernandez, Dehydration and rehydration processes of cement paste exposed to high temperature environments, J. Mater. Sci. 39 (9) (2004) 3015–3024.
[47] B.K. Marsh, R.L. Day, Pozzolanic and cementitious reactions of fly ash in blended cement pastes, Cem. Concr. Res. 18 (2) (1988) 301–310.
[48] T.L. Hughes, C.M. Methven, T.G.J. Jones, S.E. Pelham, P. Fletcher, C. Hall, Determining cement composition by Fourier transform infrared spectroscopy, Adv. Cem. Based Mater. 2 (3) (1995) 91–104.
[49] M.Y.A. Mollah, W. Yu, R. Schennach, D.L. Cocke, A Fourier transform infrared spectroscopic investigation of the early hydration of Portland cement and the influence of sodium lignosulfonate, Cem. Concr. Res. 30 (2) (2000) 267–273.
[50] S.L. Shrestha, Characterization of some cement samples of Nepal using FTIR spectroscopy, Int. J. Adv. Res. Chem. Sci. 5 (7) (2018) 19–23.
[51] R. Ylmen, U. Jäglid, Carbonation of Portland cement studied by diffuse reflection Fourier transform infrared spectroscopy, Int. J. Concr. Struct. Mater. 7 (2013) 119–125.
[52] S.K. Nath, S. Kumar, Evaluation of the suitability of ground granulated silico-manganese slag in Portland slag cement, Constr. Build. Mater. 125 (2016) 127–134.
[53] O. Burgos-Montes, M. Palacios, P. Rivilla, F. Puertas, Compatibility between superplasticizer admixtures and cements with mineral additions, Constr. Build. Mater. 31 (2012) 300–309.
[54] P.C. Hewlett. Lea's Chemistry of Cement and Concrete, 4 ed., Butterworth-Heinemann, UK, 2004.
[55] I. Soroka, Portland Cement Paste and Concrete, Macmillan International Higher Education, 1979.
[56] Tesinova, P. 2011. Advances in composite materials: analysis of natural and man-made materials: BoD–Books on Demand.
[57] A. Khelafi, N. Kaid, R. Soltani, D.E. Kerdal, H. Khelafi, Elaboration of recycled concrete sand aggregates-based mortars: an alternative recycling process, Constr. Build. Mater. 398 (2023) 132333.
[58] N. Soundarya, A review on the physical & chemical properties of sea sand to be used a replacement to fine aggregate in concrete, Mater. Today. Proc. 51 (2022) 1527–1531.
[59] I. Wilińska, B. Pacewska, A. Ostrowski, Investigation of different ways of activation of fly ash–cement mixtures: part 2—mechanical activation, J. Therm. Anal. Calorim. (2023) 1–18.
[60] P. Chindaprasirt, C. Jaturapitakkul, T. Sinsiri, Effect of fly ash fineness on microstructure of blended cement paste, Constr. Build. Mater. 21 (7) (2007) 1534–1541.
[61] I. Pane, W. Hansen, Investigation of blended cement hydration by isothermal calorimetry and thermal analysis, Cem. Concr. Res. 35 (6) (2005) 1155–1164.
[62] N. Nurmalita, S.N. Abdulmadjid, A. Setiawan, R. Idroes, Z. Jalil, Characteristics of silica powder extracted from fly ash of coal fired power plant–effect of heat treatment process, J. Ecol. Eng. 24 (9) (2023).
[63] P.S. Sidhu, R.J. Gilkes, R.M. Cornell, A.M. Posner, J.P. Quirk, Dissolution of iron oxides and oxyhydroxides in hydrochloric and perchloric acids, Clays Clay Miner. 29 (1981) 269–276.
[64] B. Šavija, M. Luković, Carbonation of cement paste: understanding, challenges, and opportunities, Constr. Build. Mater. 117 (2016) 285–301.
[65] D.P. Siriwardena, S. Peethamparan, Quantification of CO2 sequestration capacity and carbonation rate of alkaline industrial byproducts, Constr. Build. Mater. 91 (2015) 216–224.
[66] M. Thiery, G. Villain, P. Dangla, G. Platret, Investigation of the carbonation front shape on cementitious materials: effects of the chemical kinetics, Cem. Concr. Res. 37 (7) (2007) 1047–1058.
[67] M. Zajac, J. Skibsted, J. Skocek, P. Durdzinski, F. Bullerjahn, M.B. Haha, Phase assemblage and microstructure of cement paste subjected to enforced, wet carbonation, Cem. Concr. Res. 130 (2020) 105990.
[68] Ingham, J.P. 2012. Geomaterials Under the Microscope.
[69] A.B. Poole, I. Sims, Concrete Petrography: A Handbook of Investigative Techniques, Crc Press, 2016.
[70] P.Y. Loh, P. Shafigh, H.Y.B. Katman, Z. Ibrahim, S. Yousuf, pH measurement of cement-based materials: the effect of particle size, Appl. Sci. 11 (17) (2021) 8000.
[71] V. Räsänen, V. Penttala, The pH measurement of concrete and smoothing mortar using a concrete powder suspension, Cem. Concr. Res. 34 (5) (2004) 813–820.
[72] S. Cornaby, A. Reyes-Mena, H.K. Pew, P.W. Moody, T. Hughes, A. Stradling, L. V. Knight, An XRD/XRF instrument for the microanalysis of rocks and minerals, Meas. Sci. Technol. 12 (6) (2001) 676.
[73] B. Lemière, Y.A. Uvarova, New developments in field-portable geochemical techniques and on-site technologies and their place in mineral exploration, Geochem. Explor. Environ. Anal. 20 (2) (2020) 205–216.
[74] G. Chiari, P. Sarrazin, A. Heginbotham, Non-conventional applications of a noninvasive portable X-ray diffraction/fluorescence instrument, Appl. Phys. A 122 (11) (2016) 990.
[75] P. Sarrazin, G. Chiari, M. Gailhanou, A portable non-invasive XRD-XRF instrument for the study of art objects, Adv. X-ray Anal. 52 (2008) 175–186.
[76] N. Cebi, H. Bekiroglu, A. Erarslan, L. Rodriguez-Saona, Rapid sensing: Hand-held and portable FTIR applications for on-site food quality control from farm to fork, Molecules 28 (9) (2023) 3727.
[77] I. Yut, A. Zofka, Fingerprinting of chemical admixtures in fresh portland cement concrete by portable infrared spectrometer, Transp. Res. Rec. 2290 (1) (2012) 1–9.
[78] E.L. Ashley, E. Cauda, L.G. Chubb, D.P. Tuchman, E.N. Rubinstein, Performance comparison of four portable FTIR instruments for direct-on-filter measurement of respirable crystalline silica, Ann. Work Expo. Health 64 (5) (2020) 536–546.